Astrocytic Kir4.1 channels regulate locomotion by orchestrating neuronal rhythmicity in the spinal network

Tony Barbay, Emilie Pecchi, Myriam Ducrocq, Nathalie Rouach, Frédéric Brocard, Rémi Bos

Received: 18 August 2022 | Revised: 22 December 2022 | Accepted: 2 January 2023

DOI: 10.1002/glia.24337

GLIA

WILEY

RESEARCH ARTICLE

Astrocytic Kir4.1 channels regulate locomotion by orchestrating neuronal rhythmicity in the spinal network

Tony Barbay[1] | Emilie Pecchi[1] | Myriam Ducrocq[1] | Nathalie Rouach[2] | Frédéric Brocard[1] | Rémi Bos[1]

[1]Aix Marseille Univ, CNRS, Institut de Neurosciences de la Timone (INT), UMR 7289, Marseille, France

[2]Center for Interdisciplinary Research in Biology, Collège de France, CNRS, INSERM, Labex Memolife, Université PSL, Paris, France

Correspondence
Rémi Bos, Aix Marseille Univ, CNRS, Institut de Neurosciences de la Timone (INT), UMR 7289, Marseille, France.
Email: remi.bos@univ-amu.fr

Funding information
Agence Nationale de la Recherche, Grant/Award Number: ANR-16-CE16-0004; Centre National de la Recherche Scientifique, Grant/Award Number: FI_INT_JCJC_2019; Ministère de l'Enseignement Superieur, de la Recherche et de l'Innovation, Grant/Award Number: MESRI_2021_BARBAY

Abstract

Neuronal rhythmogenesis in the spinal cord is correlated with variations in extracellular K^+ levels ($[K^+]_e$). Astrocytes play important role in $[K^+]_e$ homeostasis and compute neuronal information. Yet it is unclear how neuronal oscillations are regulated by astrocytic K^+ homeostasis. Here we identify the astrocytic inward-rectifying K^+ channel Kir4.1 (a.k.a. *Kcnj10*) as a key molecular player for neuronal rhythmicity in the spinal central pattern generator (CPG). By combining two-photon calcium imaging with electrophysiology, immunohistochemistry and genetic tools, we report that astrocytes display Ca^{2+} transients before and during oscillations of neighboring neurons. Inhibition of astrocytic Ca^{2+}-transients with BAPTA decreases the barium-sensitive Kir4.1 current responsible of K^+ clearance. Finally, we show in mice that Kir4.1 knockdown in astrocytes progressively prevents neuronal oscillations and alters the locomotor pattern resulting in lower motor performances in challenging tasks. These data identify astroglial Kir4.1 channels as key regulators of neuronal rhythmogenesis in the CPG driving locomotion.

KEYWORDS
astrocytes, Kir4.1, locomotion, neuronal oscillations, potassium clearance, spinal cord

1 | INTRODUCTION

Mammalian locomotion relies on repeated sequences of muscle contractions triggered by a rhythmic central pattern generator (CPG) network, which is mainly located in the ventromedial part of the lumbar spinal cord (Grillner & El Manira, 2020; Kiehn, 2016). Activation of the spinal CPG network is triggered by descending inputs releasing neuromodulators such as glutamate, serotonin and dopamine. Several populations of CPG interneurons—V0, V2a and Hb9—display conditional rhythmic oscillations in response to neuromodulators (Grillner & El Manira, 2020; Kiehn, 2016). No single population of ventromedial interneurons appears to act alone or to orchestrate the entire CPG pattern. The spinal rhythmogenesis emerges from the synchronization of individual neurons with intrinsic bursting properties (Brocard et al., 2010). Despite decades of research, the functional organization of the locomotor CPG remains still unclear.

In the spinal locomotor CPG, physiological variation in extracellular K^+ ($[K^+]_e$) coincides with the emergence of the oscillatory pattern of intrinsic bursting neurons (Brocard et al., 2013), and thus powers up the motor output (Bos et al., 2018; Bracci & Nistri, 1998). At rest, $[K^+]_e$ is kept close to 3 mM in serum levels (Kofuji & Newman, 2004; Verkhratsky et al., 2018). The maintenance of K^+ homeostasis is one of the crucial supportive functions mediated by astrocytes (Ben Haim et al., 2015; Sibille et al., 2015). In addition, to display a high resting K^+

Tony Barbay and Emilie Pecchi contributed equally to this work.

conductance that facilitates the uptake of neuron released K^+, astrocytes have a hyperpolarized resting membrane potential (RMP). Both parameters rely on the activity of the weakly inwardly rectifying Kir4.1 K^+ channel, which in the nervous system is expressed exclusively in glial cells, with the highest expression in astrocytes (Kelley et al., 2018). Astrocytic Kir4.1 channels have been described in many CNS regions, including the spinal cord (Olsen et al., 2006; Ransom & Sontheimer, 1995). Studies using genetic, pharmacological and modeling approaches in the brain networks identified Kir4.1 as the main astrocytic inwardly rectifying K^+ channel regulating $[K^+]_e$ and thus influencing neuronal excitability (Nwaobi et al., 2016; Sibille et al., 2015).

Astrocytes display ramified processes enwrapping synapses, placing them in an ideal position to (i) sense synaptic activity (Panatier et al., 2011) and (ii) adjust network activity by releasing gliotransmitters (Araque et al., 2014; Savtchouk & Volterra, 2018). Rhythmic oscillations are strongly affected in brain networks when gliotransmission is genetically or pharmacologically modified (Lee et al., 2014; Sheikhbahaei et al., 2018). In the spinal motor network, the locomotor oscillatory rhythm is correlated with enhanced calcium (Ca^{2+}) transients in astrocytes (Broadhead & Miles, 2020), which likely triggers ATP release (Witts et al., 2015), modulating excitatory synaptic transmission (Carlsen & Perrier, 2014). Thus, growing evidence point to the contribution of gliotransmission in modulating neuronal rhythmogenesis (Montalant et al., 2021). Astrocytes can also respond to neurotransmitters and neuromodulators (Paukert et al., 2014; Rosa et al., 2015) by modifying $[K^+]_e$, which greatly impact brain oscillations (Bellot-Saez et al., 2018; Ding et al., 2016; Sibille et al., 2015). However, the mechanisms underlying the contribution of astrocytic K^+ homeostasis to rhythmogenesis remain incompletely understood.

Here we investigated whether astrocyte K^+ uptake modulates neuronal oscillations patterns in the spinal CPG network. We demonstrate that most of the ventromedial astrocytes are active during neuronal oscillations, and that the inwardly-rectifying Kir4.1 channels are crucial for maintaining neuronal oscillations, which ultimately influence the locomotor activity. This study places astrocytes as central elements of the spinal cord locomotor CPG.

2 | MATERIALS AND METHODS

2.1 | Experimental model

2.1.1 | Mice

Mice of either sex (P3–P4 for fictive locomotion experiments, P5–P14 for Patch-clamp recording, P13–P16 for two-photon Ca^{2+} imaging, P12–P13 for swimming tests, P14–P15 for rotarod tests, P14–P18 for Catwalk tests) were housed under a 12 h light/dark cycle in a temperature-controlled area with ad libitum access to water and food. Hb9-eGFP mice (C57/Bl6 background) expressing GFP in ventromedial oscillatory interneurons were provided by the Jackson laboratory (Strain #005029) and the *Aldh1L1*-eGFP mice (CD1 background) expressing GFP in astrocytes were kindly provided by Nathalie Rouach (Collège de France, CNRS, INSERM, Labex Memolife, Université PSL, Paris, France). Animals from different litters were used for each experiment. Sample sizes (number of spinal cords and/or cells) for each experiment are indicated in figure legends. All animal care and use were conformed to the French regulations (Décret 2010-118) and approved by the local ethics committee (Comité d'Ethique en Neurosciences INT-Marseille, CE71 Nb A1301404, authorization Nb 2018110819197361).

2.2 | Experimental procedures

2.2.1 | shRNA constructs

Specific shRNA sequence designed to knockdown *Kir4.1* transcript (Cui et al., 2018) was incorporated into an adeno-associated viral (AAV) vector (serotype 9), which features a H1 promoter to drive shRNA expression and a CAG promoter to drive eGFP expression for identification of transduced cells (Cui et al., 2018). We also used a non-targeting shRNA sequence (Luciferase) which has no homology to any known genes in mouse as a control. AAV were produced following standard protocols (Molecular Cloning, A Laboratory Manual, Fourth Edition, 2012) with minor modifications. Briefly, HEK293T cells were transfected with the three plasmids (pRC, pHelper and pAAV) using the $MgCl_2$ method. After 60–72 h, AAV particles from the cells and the medium were recovered and concentrated using Takara AAV-Purification All serotypes kit (Takara). We systematically included a digestion step with cryonase to degrade non-encapsidated viral genomes. Viral particles were quantified using quantitative PCR (Takara Titration kit). Vectors titers range was between 2×10^{11} and 3×10^{12} vectors/ml.

2.2.2 | Intrathecal vector delivery

A minimally-invasive technique was used to micro-inject adeno-associated viral (AAV) vectors into the T13-L1 intervertebral space. Briefly, in pups cryoanesthetized at birth, the intervertebral space was widened by flexing the spine slightly. The tip of the microcapillary preloaded with the AAV particles was lowered into the center of the T13-L1 intervertebral space. A total volume of 2 µl /animal was then progressively injected (1 µl/5 s).

2.2.3 | Ex vivo preparations and aCSF solutions

i. *For the slice preparation*, the lumbar spinal cord was isolated in ice-cold (+4°C) artificial cerebro-spinal fluid (aCSF) solution composed of the following (in mM): sucrose (252), KCl (3), NaH_2PO_4 (1.25), $MgSO_4$ (4), $CaCl_2$ (0.2), $NaHCO_3$ (26), D-glucose (25), pH 7.4. The lumbar spinal cord was then introduced into a 4% agar solution, quickly cooled, mounted in a vibrating microtome (Leica, VT1000S) and sliced (325 µm) through the L1–2 lumbar segments. Slices were immediately transferred into the holding chamber filled with bubbled (95% O_2 and 5% CO_2) standard aCSF composed of

(in mM): NaCl (120), KCl (3), NaH_2PO_4 (1.25), $MgSO_4$ (1.3), $CaCl_2$ (1.2), $NaHCO_3$ (25), D-glucose (20), pH 7.4, 30–32°C. After a 30–60 min resting period, individual slices were transferred to a recording chamber continuously perfused with standard aCSF heated to 32–34°C. The oscillatory aCSF characterized by higher extracellular K^+ and lower Ca^{2+} (Brocard et al., 2013) was composed of the following (in mM): NaCl (120), KCl (6), NaH_2PO_4 (1.25), $MgSO_4$ (1.3), $CaCl_2$ (0.9), $NaHCO_3$ (25), D-glucose (20). The rhytmogenic cocktail (Ziskind-Conhaim et al., 2008) that we called neuromodulator cocktail in this study, was composed of the following (in µM): tetrodotoxin (TTX, 0.5–1), N-methyl-D-aspartate (NMDA, 20), *5-hydroxytryptamine (5-HT, 20)*, dopamine (DA, 50).

ii. *For the whole-spinal cord preparation*, the spinal cord was transected at T8-9, isolated and transferred with intact dorsal and ventral roots to the recording chamber. The tissue was continuously bubbled (95% O_2 and 5% CO_2) and perfused with heated (~27–28°C) standard aCSF solution composed of (in mM): 120 NaCl, 4 KCl, 1.25 NaH_2PO_4, 1.3 $MgSO_4$, 1.2 $CaCl_2$, 25 $NaHCO_3$, 20 D-glucose, pH 7.4. The oscillatory aCSF was composed as described above. The neuromodulator cocktail was composed of the following (in µM): N-methyl-DL-aspartate (NMA, 12), *5-hydroxytryptamine (5-HT, 5)*.

2.2.4 | Ex vivo recordings

i. *For the slice preparation*, whole-cell patch-clamp recordings of L1–L2 ventromedial interneurons and astrocytes were performed using a Multiclamp 700B amplifier (Molecular Devices). The apparatus was equipped with two headstages, allowing recordings of pairs of cells. Patch electrodes (4–5 MΩ for neurons) were pulled from borosilicate glass capillaries (1.5 mm OD, 1.12 mm ID; World Precision Instruments) on a Sutter P-97 puller (Sutter Instruments Company) and filled with an intracellular solution (in mM): K^+-gluconate (140), NaCl (5), $MgCl_2$ (2), HEPES (10), EGTA (0.5), ATP (2), GTP (0.4), pH 7.3. For GFP+ astrocyte recordings, pipettes (7–9 MΩ) were filled with an intracellular solution (in mM): K^+-gluconate (105), NaCl (10), KCl (20), $MgCl_2$ (0.15), HEPES (10), EGTA (0.5), ATP (4), GTP (0.3), pH 7.3. In some recordings, 30 mM of BAPTA was added in the pipette solution to chelate intracellular free Ca^{2+} from the intracellular stores. In some experiments, GFP negative astrocytes were identified on the basis of their morphology (i.e., small somata with a diameter of <10 µm surrounded by many processes) and their electrophysiological properties (i.e., a hyperpolarized RMP (<−75 mV), a linear I/V relationship, no spike in response to increased injection currents and a low input resistance (<100 MΩ)). When GFP negative, some astrocytes were filled with Alexa Fluor® 488 or 594 (25 µM) diluted in the intracellular solution. Pipette and neuronal capacitive currents were canceled and, after breakthrough, the series resistance was compensated and monitored. Recordings were digitized on-line and filtered at 10 kHz (Digidata 1550B, Molecular Devices). All experiments were designed to gather data within a stable period (i.e., at least 1–2 min after establishing whole-cell access).

ii. *For the whole spinal cord preparation*, motor outputs were recorded from L2 lumbar ventral roots by means of glass suction electrodes connected to an AC-coupled amplifier. Signals from the electrodes placed in contact with the ventral root recordings were amplified (×2000), high-pass filtered at 70 Hz, low-pass filtered at 3 kHz, and sampled at 10 kHz. Custom-built amplifiers enabled simultaneous online rectification and integration (100 ms time constant) of raw signals. Locomotor-like activity was induced by (i) rising $[K^+]_e$ to 6 mM and decreasing $[Ca^{2+}]_e$ to 0.9 mM (oscillatory aCSF, see above) or (ii) bath application of the neuromodulator cocktail composed of N-methyl-DL aspartate (NMA, 12 µM) and 5-hydroxytryptamine (5-HT, 5 µM).

2.2.5 | Two-photon Ca^{2+} imaging

Two-photon fluorescence measurements were obtained with a dual-scanhead two-photon microscope (FemtoS-Dual, Femtonics Ltd, Budapest, Hungary) and made using an Olympus XLUMPlanFL N 20×, 1.00 (Olympus America, Melville, NY). Two-photon excitation of Gcamp6f and jRGECO1a was simultaneously evoked with a femtosecond pulsed laser (Chameleon Ultra II; Coherent, Santa Clara, CA) tuned to 960 nm. In some experiments, slices were loaded with the Ca^{2+} indicator Rhod-2 AM (10 µM, Invitrogen; #R1245MP) which preferentially label astrocytes (Carlsen et al., 2021; Otsu et al., 2015) at 32–34°C for 1 h, in dark, with 0.02% Pluronic F-127 (Merck Sigma-Aldrich; #P2443) 0.2% DMSO (Merck Sigma-Aldrich; #D4540) in standard bubbled aCSF. After incubation, slices were washed for at least 15 min to allow the de-esterification of the dye. For Rhod-2 AM experiments fluorophore was excited at 840 nm and astrocytes were identify based on their small size (~10 µm) and characteristic morphology of a round soma surrounded by many processes.

The microscope system was controlled by MESc acquisition software (https://femtonics.eu/femtosmart-software/, Femtonics Ltd, Budapest, Hungary). A single acquisition plane was selected and full-frame imaging was started in a resonant scanning mode at 30.5202 Hz. Scan parameters were [pixels/line × lines/frame (frame rate in Hz)]: [512 × 519 (30.5202)]. Scanning area was 468 µm × 474 µm. This microscope was equipped with two detection channels for fluorescence imaging.

2.2.6 | Immunohistochemistry

Spinal cords of 10 to 12-day-old mice were dissected out and fixed for 5–6 h in 4% paraformaldehyde (PFA), then rinsed in phosphate buffered saline (PBS) and cryoprotected overnight in 20% sucrose at 4°C. Spinal cords were frozen in OCT medium (Tissue Tek) and 30 µm cryosections were collected from the L1–L2 segments. After having been washed in PBS 3 × 5 min, the slides were incubated for 1 h in a blocking solution (BSA 1%, Normal Donkey Serum 3% in PBS) with

0.2% triton X-100 and for 48 h at 4°C in a humidified chamber with the primary antibody anti-Kir4.1 (Alomone, #APC035, 1/1000) or for 12 h at 4°C with the primary antibody anti-NeuN (Merck Millipore, #MAB377, 1/200), or for 12 h at 4°C with the primary antibody anti-MMP9 (Merck Sigma-Aldrich, #M9570, 1/500). All antibodies were diluted in the blocking solution with 0.2% triton X-100. Slides were then washed 3 × 5 min in PBS and incubated for 2 h with an Alexa Fluor® Plus 555- conjugated secondary antibody (Invitrogen #A32794, 1/400), an Cy5-conjugated secondary antibody (Jackson ImmunoResearch, #715-175-151, 1/400) or Alexa Fluor® Plus 555-conjugated secondary antibody (Invitrogen #A32816, 1/400) diluted in the blocking solution. After three washes of 5 min in PBS, they were mounted with a gelatinous aqueous medium containing Hoechst 33342 (ThermoFisher, #62249, 1/10000, initial concentration: 20 mM). Images were acquired using a confocal microscope (LSM700, Zeiss) equipped with either a 20× air objective, a 40× oil objective or a 63× oil objective and processed with the Zen software (Zeiss).

2.2.7 | Kir4.1 protein analysis by capillary western blot

The lumbar parts of the spinal cords were dissected in standard aCSF at 4°C and conserved at −80°C until protein extraction. Tissues were homogenized in ice-cold lysis buffer (250 mM sucrose, 3.9 mM Tris pH 7.5, 10 mM iodoacetamide) supplemented with protease inhibitors (cOmplete™, Mini, EDTA-free Protease Inhibitor Cocktail, Roche 11836170001). Unsolubilized material was pelleted by centrifugation at 7000×*g* for 5 min at 4°C and discarded. The supernatants were subjected to an additional centrifugation step at 19,000 x g for 70 min at 4°C. The resulting pellets corresponding to the membrane-enriched fraction were resuspended in ice-cold lysis buffer (PBS 1×, 1% IGEPAL® CA-630 1%, SDS 0.1%) supplemented with protease inhibitors (cOmplete™, Mini, EDTA-free Protease Inhibitor Cocktail, Roche 11836170001). Protein concentrations were determined using the Pierce™ BCA Protein Assay Kit (ThermoFisher 23227). Kir4.1 expression was then analyzed using the 12–230 kDa separation module (SM-W004 ProteinSimple) on an automated capillary western blotting system ('Jess' ProteinSimple) according to the manufacturer's protocol with small modifications. Samples were not implemented with DTT and they were not submitted to heat denaturation in order to keep proteins in a more 'native' form. A total protein concentration of 0.1 mg/ml was used. Samples were probed with a rabbit polyclonal Kir4.1 antibody (1:60; Alomone APC-035) and revealed with the appropriate detection module (DM-001 ProteinSimple). Loaded samples were normalized to their own total protein content using the 'total protein detection module' (DM-TP01 ProteinSimple).

2.2.8 | Assessment of in vivo motor behaviors

i. *Walking*. The CatWalkXT (Noldus Information Technology, Netherlands) was used to measure walking performance. Each animal walked freely through a corridor on a glass walkway illuminated with beams of light from below. A successful walking trial was defined as having the animal walk at a steady speed (no stopping, rearing, or grooming), and three to five successful trials were collected per animal. The footprints were recorded using a camera positioned below the walkway, and footprint classification was manually corrected to ensure accurate readings. The paw print parameters were then analyzed using the CatWalk software (see Section 2.3).

ii. *Rotarod test*. Mice were placed on a rotarod (Bioseb) rotating at an accelerating from 4 to 40 rpm over a span of 5 min. Mice were given three trials with a 60 s inter-trial interval.

iii. *Swimming*. Mice were gently placed individually in the center of the tank (~19,000 cm^3) filled with heated water (30–33°C). Swimming distance and velocity were quantified during three consecutive 90 s periods. Each trial was spaced by a 10 min interval. At the end of the trial, the mouse was immediately removed from the tank, dried off with a paper towel, and returned to its home cage. Swimming parameters tracking and analysis were performed by using an automated video-tracking Ethovision system (Noldus). All behavioral experiments were carried out with the experimenter blind to genotype.

2.2.9 | Drugs

All solutions were oxygenated with 95% O_2/5% CO_2. All salt compounds, *N*-methyl-*D*-aspartic acid (NMDA, 20 µM; #M3262), dopamine hydrochloride (DA, 50 µM; #H8502) *N*-methyl-DL-aspartic acid (NMA, 12 µM; #M2137), 5-hydroxytryptamine creatinine sulfate (5-HT, 5–20 µM; #S2805), Barium chloride dihydrate (Ba^{2+}, 100 µM; #217565), and 1,2-bis(o-aminophenoxy)ethane-*N*,*N*,*N*′,*N*′-tetraacetic acid (BAPTA, 30 mM; #A9801) were obtained from Merck Sigma-Aldrich. Tetrodotoxin (TTX, 0.5-1 µM; #1078) from Tocris Bioscience. All drugs were dissolved in water and added to the standard aCSF.

2.3 | Data analysis

Electrophysiological data analyses were analyzed off-line with Clampfit 10.7 software (Molecular Devices).

i. For *intracellular recordings*, several basic criteria were set to ensure optimum quality of intracellular recordings. Only cells exhibiting a stable RMP, access resistance (<20% variation) and an action potential amplitude larger than 40 mV were considered. Passive membrane properties of cells (neurons and astrocytes) were measured by determining from the holding potential the largest voltage deflections induced by small current pulses that avoided activation of voltage-sensitive currents. We determined input resistance by the slope of linear fits to voltage responses evoked by small positive and negative current injections. All reported membrane potentials were corrected for liquid junction

potentials (+14 mV for neurons and +11.4 mV for astrocytes). To activate Kir-currents in spinal astrocytes, voltages were repeatedly stepped from −140 to 50 mV, in 10 mV increments. Astrocytes were initially clamped at their RMP. 100 μM Ba^{2+} was bath applied to the slice approximately 5 min after the start of the recording. The current amplitude was measured as the difference between the baseline level before the initial voltage step, and the mean amplitude over a 10 ms window starting 10 ms after onset of the hyperpolarizing voltage step. The Ba^{2+} sensitive current was obtained by subtracting the current after Ba^{2+} application from the current before application.

ii. For *extracellular recordings*, alternating activity between right/left L2 recordings was taken to be indicative of fictive locomotion. To characterize locomotor burst parameters (during 1–2 mins of steady state), raw extracellular recordings from ventral roots were rectified, integrated and resampled at 50 Hz. Peak amplitude and duration of locomotor burst were measured by using a threshold function and the cycle period was calculated by measuring the time between the first two peaks of the autocorrelogram. The coupling between right/left L2 was estimated by measuring the correlation coefficient of the cross-correlogram at zero phase lag.

2.3.1 | Analysis of firing patterns

Firing patterns of GFP+ interneurons were characterized as tonic or rhythmic bursting discharge in response to ions variations before or after pharmacological or genetic blockade of Kir.1 channels. Tonic discharge typically consisted of low-frequency single spikes (<10 Hz) separated by regular but relatively long intervals (interspike intervals: ISI of 200–600 ms). We defined bursts as depolarizing plateaus over-ridden by at least two actions potentials followed by a silent period. The period separating the beginning of two consecutive plateaus was used to calculate the inter-burst frequency in intracellular recordings. Bursting frequency was calculated only in neurons that displayed a stable rhythmic discharge for more than five cycles.

2.3.2 | Two-photon Ca^{2+} imaging analyses

Fluorescent time series depicting the Ca^{2+} changes occurring ex vivo in both the neurons and the astrocytes were analyzed with the MESc data acquisition software (Femtonics Ltd, Budapest, Hungary) and the MES curve analyzer tool. Briefly, regions of interest (ROIs) were manually selected based on the appearance of Ca^{2+} transients in the time series images. A signal was declared as a Ca^{2+} transient if it exceeded the baseline by greater than twice the baseline noise (SD). ROIs coincide with (i) active dendritic components for neurons, (ii) active microdomains or territories from the astrocytic processes in Gcamp6f experiments and (iii) active soma or main processes in Rhod-2 AM experiments. Astrocyte territory sizes were estimated by measuring the area of a ROI that surrounded the largest fluorescence projection profile of bushy astrocytes gathered from a series of z-stack images. The astrocytic ROIs were separated at least by a distance of 60 μm. The raw fluorescence Ca^{2+} traces were extracted to Excel and analyzed using custom Matlab scripts. They were transformed to show fluorescence change according to Equation (1):

$$\Delta F/F = (F_1 - F_0)/F_0, \quad (1)$$

where F is the fluorescence at any given point in time, and F_0 is the mean fluorescence value for the 5–10 s range, preceding the bath perfusion of the oscillatory aCSF or the neuromodulator cocktail. Following this, the signal-to-noise ratio (SNR) is:

$$\mathrm{SNR} = (\Delta F/F)_{\mathrm{peak}}/\sigma F,$$

where σF is the standard deviation of the baseline period. We took those events as a Ca^{2+} response that exceeded the threshold of two times the standard deviation of the baseline period. The peak amplitude, duration and frequency of the Ca^{2+} transients were analyzed by using a Matlab script. In each FOV where dorsal is up and ventral is down, all astrocytic Ca^{2+} transients above the central canal were considered as dorsal astrocytic activity and distinguished from the ventral astrocytic Ca^{2+} transients.

2.3.3 | In vivo behavioral analyses

For walking, the CatWalk XT software (Noldus Information Technology, Netherlands) was used to measure a broad number of spatial and temporal gait parameters in several categories. These include (i) dynamic parameters related to individual paw prints, such as duration of the step cycle with the respective duration of the swing and stance phases; (ii) parameters related to the position of paw prints with respect to each other, for example the stride length (distance between two consecutive placement of the same paw) and the base of support (the width between the paw pairs); (iii) parameters related to time-based relationships between paw pairs, as well as step patterns. These parameters were calculated for each run and for each paw. In the rotarod test the average latency of the subject to fall was recorded (in seconds). A video tracking system (Noldus Information Technology, Wageningen, The Netherlands) was used to measure swimming performance. We ensured there was a smooth tracking curve and that the center point of the animal remained stable before analysis took place. Distance and velocity during the test periods were scored. All behavioral tests were carried out with the experimenter blind to genotype.

2.4 | Experimental design and statistical analysis

No statistical method was used to predetermine sample size. Group measurements were expressed as mean ± SEM. When two groups

were compared, we used the Mann–Whitney test. Fisher test was used to compare the percentages of oscillatory neurons. When two conditions (control vs drugs) were compared, we used the Wilcoxon matched pairs test. We also used a one-way or two-way ANOVA tests for multiple comparisons. For all statistical analyses, the data met the assumptions of the test and the variance between the statistically compared groups was similar. The level of significance was set at $p < .05$. Statistical analyses were performed using Graphpad Prism 9 software. They are all indicated in Figure legends and in Source data file.

3 | RESULTS

3.1 | Astrocytes respond to changes in extracellular ions underlying neuronal oscillations in the spinal CPG

Astrocytes from the ventromedial part of upper lumbar segments (L1–L2), the main locus of the locomotor CPG (El Manira, 2014; Kiehn, 2016), were recorded from transgenic mice expressing GFP under the control of the astrocytic *Aldh1L1* promoter (Tsai et al., 2012) (Figure 1a). This spinal region contains interneurons endowed with two types of inherent membrane oscillations at a frequency range similar to stepping rhythms: (i) one is mainly dependent on the persistent sodium current (INaP) (Tazerart et al., 2008) sensitive to tetrodotoxin (TTX), the voltage-dependent sodium channels blocker, and triggered by a rise in $[K^+]_e$ with a concomitant decrease in extracellular Ca^{2+} levels ($[Ca^{2+}]_e$) (Brocard et al., 2013), (ii) the other is TTX-insensitive dependent on the Ca^{2+} currents and triggered by a neuromodulator cocktail composed of 5-HT, dopamine and NMDA, in presence of TTX (Masino et al., 2012; Wilson et al., 2005; Ziskind-Conhaim et al., 2008). This neuromodulator cocktail mimics the effect of descending inputs from the hindbrain for inducing a locomotor rhythmicity (Grillner & El Manira, 2020). In recording conditions required to generate bursting cells, all astrocytes displayed a reversible depolarisation of their membrane potentials: (i) when $[K^+]_e$ was increased to 6 mM and $[Ca^{2+}]_e$ decreased to 0.9 mM (Figure 1b,c) or (ii) when the neuromodulator cocktail was applied in presence of TTX (Figure 1d,e). We observed that in absence of neuronal activity, neuromodulators increased $[K^+]_e$ to ~6 mM (Figure S1). To explore the temporal dynamics of the astrocytic response compared to neuronal oscillations, we performed dual recordings of a ventromedial Hb9 GFP+ interneuron which is known to display the two types of bursting properties (Tazerart et al., 2008; Ziskind-Conhaim et al., 2008) and an adjacent astrocyte from the upper lumbar segments (L1–L2) (Figure 1f). In 13 pairs, astrocytic depolarization in response to the TTX-sensitive $[K^+]_e$/$[Ca^{2+}]_e$ variations (Figure 1g) or the TTX-insensitive neuromodulator cocktail (Figure 1h) either preceded (69%) or followed (31%) the onset of the neuronal rhythmic bursting of the adjacent GFP+ pacemaker interneurons (Figure 1i), suggesting that astrocytes play an active role in spinal rhythmogenesis.

3.2 | Enhanced astrocytic Ca^{2+} transients occur during neuronal oscillations in the ventral spinal cord

To better locate and characterize the dialogue between neurons and astrocytes during spinal oscillations, we performed two-photon Ca^{2+} imaging of neuronal and astrocyte signals in the locomotor CPG area. Mice were injected at birth with adeno-associated virus serotype 9 (AAV9) (Figure 2a) designed to express GCaMp6f in astrocytic processes under the gfaABC1D promoter and jRGECO1a in neurons under the Syn.NES promoter (Figure 2b). We simultaneously imaged the chromophores in lumbar slices (L1-L2) of post-natal mice (day 13–16) and first confirmed that neuronal signals were prevented by TTX, in contrast to the signals recorded in astrocyte processes that remain intact (Figure 2c,d).

We next explored the spatio-temporal dynamics of the astrocytic transients and compared it to the neuronal transients. In response to changes in extracellular K^+ and Ca^{2+} levels or bath application of the neuromodulator cocktail in presence of TTX, neurons displayed Ca^{2+} oscillatory transients (0.16 ± 0.03 and 0.15 ± 0.01 Hz, respectively) (Figure 3a,b), which correlated with enhanced astrocytic Ca^{2+} transients in processes (Figure 3a,c). Interestingly, we distinguished distinct subsets of astrocytic Ca^{2+} signals. Some astrocytes showed increased Ca^{2+}transients before the onset of the neuronal Ca^{2+} oscillations, in contrast to others, which displayed Ca^{2+} transients during neuronal oscillations (Figure 3a). Quantification showed that the occurrence of Ca^{2+} transients preceded the neuronal oscillations in ~64% of astrocytes, whereas in ~36% of them the Ca^{2+} transients occurred during neuronal oscillations (Figure 3d). These data confirmed our electrophysiological dual recordings (Figure 1i). We also observed that most of the astrocytes (~70%) showing Ca^{2+} signal increases in response to ionic variations or perfusion of the neuromodulator cocktail were located in the ventromedial part of the spinal cord (Figure 3e). Altogether, these data suggest that ventromedial astrocytes are functionally coupled with neuronal rhythmicity in the spinal CPG area.

3.3 | The astrocytic Ca^{2+} transients regulate the Kir4.1-mediated inwardly rectifying K^+ current

Because astrocytic Ca^{2+} signals modulate $[K^+]_e$ in hippocampus (Wang, Smith, et al., 2012) and cerebellum (Wang, Xu, et al., 2012), we then investigated whether the increase in astrocytic Ca^{2+} transients related to neuronal oscillations in the spinal CPG area stimulates K^+ uptake. We first recorded the passive membrane properties of the ventromedial GFP+ astrocytes from upper lumbar slices (Figure 4a,b) and then isolated the Ba^{2+}-sensitive Kir4.1 current underlying K^+ uptake in standard aCSF (Figure 4c,d). We then switched to oscillatory aCSF by increasing $[K^+]_e$ to 6 mM and reducing $[Ca^{2+}]_e$ to 0.9 mM, which leads to neuronal bursting (Figure 1g; Figure 3a,b) and intracellular astrocytic Ca^{2+} transients (Figure 3a,c). In this condition, we first observed a higher barium (Ba^{2+})-sensitive current driven by Kir4.1 channels compared to standard aCSF

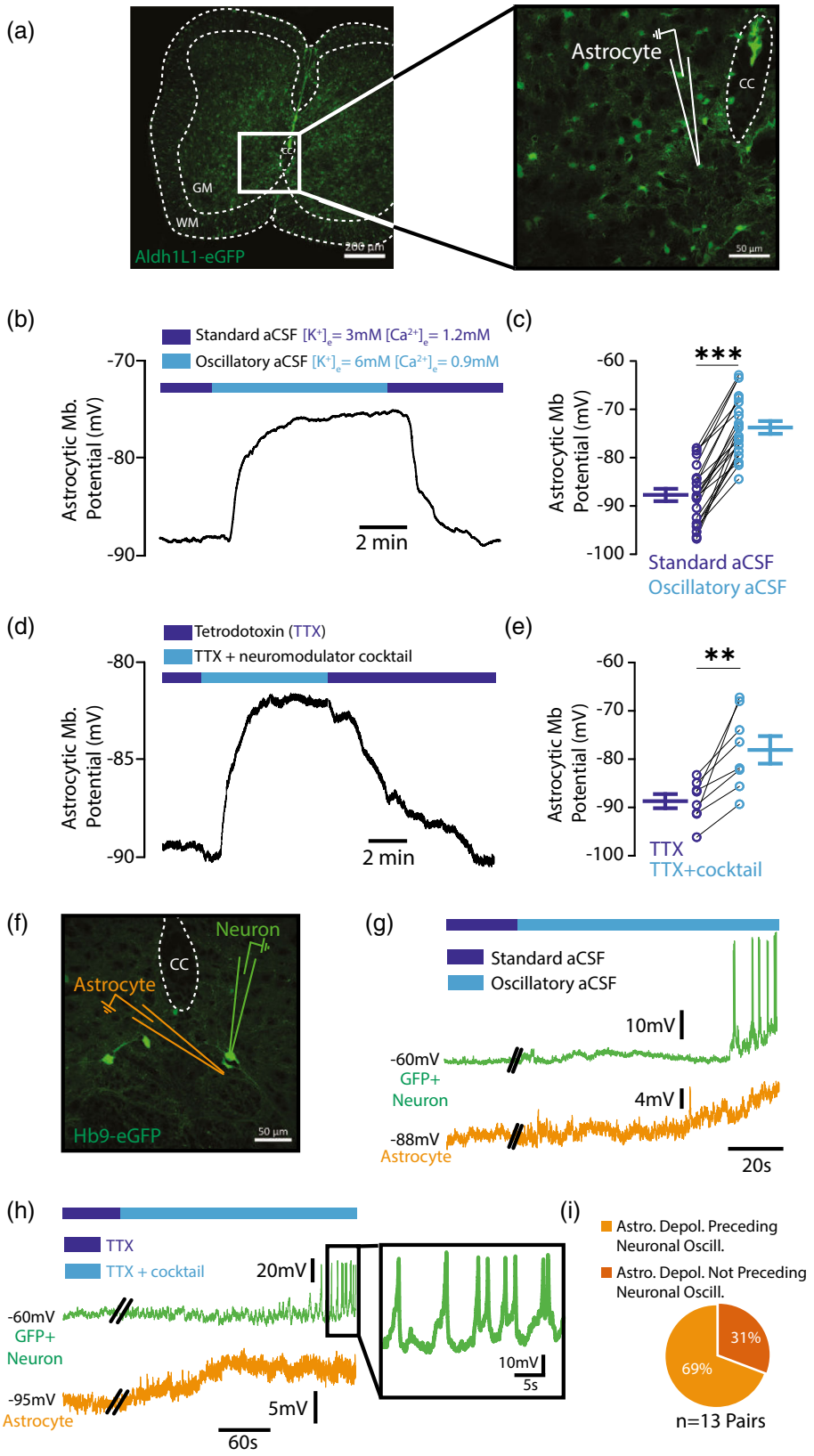

FIGURE 1 Astrocytes respond to variations in $[K^+]_e$ and $[Ca^{2+}]_e$ related to neuronal oscillations in the spinal CPG. (a) Confocal image of endogenous GFP from a lumbar slice of a P8 *Aldh1L1-eGFP* mouse. White inset represents the patch-clamp recording area of the ventromedial GFP+ astrocytes. The recording glass microelectrode is in white. CC stands for central canal, GM for gray matter and WM for white matter. (b) Representative voltage trace of a GFP+ astrocyte in response to $[K^+]_e$ rise to 6 mM and $[Ca^{2+}]_e$ decrease to 0.9 mM. (c) Quantification of the effect of the $[K^+]_e$ and $[Ca^{2+}]_e$ variations on the astrocytic membrane potential ($n = 22$ astrocytes from 16 mice). (d) Representative voltage trace of a GFP + astrocyte in response to bath application of a neuromodulator cocktail (dopamine, serotonin, and NMDA) in presence of TTX. (e) Quantification of the effect of the neuromodulator cocktail on the astrocytic membrane potential ($n = 8$ astrocytes from 4 mice). (f) Confocal image of the endogenous GFP from the ventromedial part of a lumbar slice of a P12 Hb9-eGFP mouse. The green and orange glass microelectrodes represent the dual recording of a GFP+ interneuron and an adjacent astrocyte, respectively. CC for central canal. (g,h) The $[K^+]_e$ and $[Ca^{2+}]_e$ variations (g, light blue) or the bath application of the neuromodulator cocktail in presence of TTX (h, light blue) induces bursting in Hb9 GFP+ interneurons (green traces) preceded by a depolarization of the neighboring astrocyte (orange traces). The black inset in (h) represents the TTX-insensitive neuronal oscillations. (i) Proportion of the astrocytic membrane potential depolarization preceding (light orange) or not preceding (dark orange) the onset of neuronal bursting ($n = 13$ pairs from 8 mice). $^{**}p < 0.01$; $^{***}p < 0.001$ (two-tailed Wilcoxon paired test for (c) and (e). Mean ± SEM. For detailed *p* values, see Source data file

(Figure 4c-g). Then, in contrast to what we found in the standard aCSF condition (Figure 4c,d,g), preventing the astrocytic Ca^{2+} transients with intracellular BAPTA (30 mM) delivered via the patch pipette in the oscillatory aCSF condition significantly reduced the barium (Ba^{2+})-sensitive current driven by Kir4.1 channels (Figure 4e-g). These data strongly suggest that the increased intracellular Ca^{2+} from ventromedial astrocytes during neuronal oscillations modulates K^+ uptake via Kir4.1 channels.

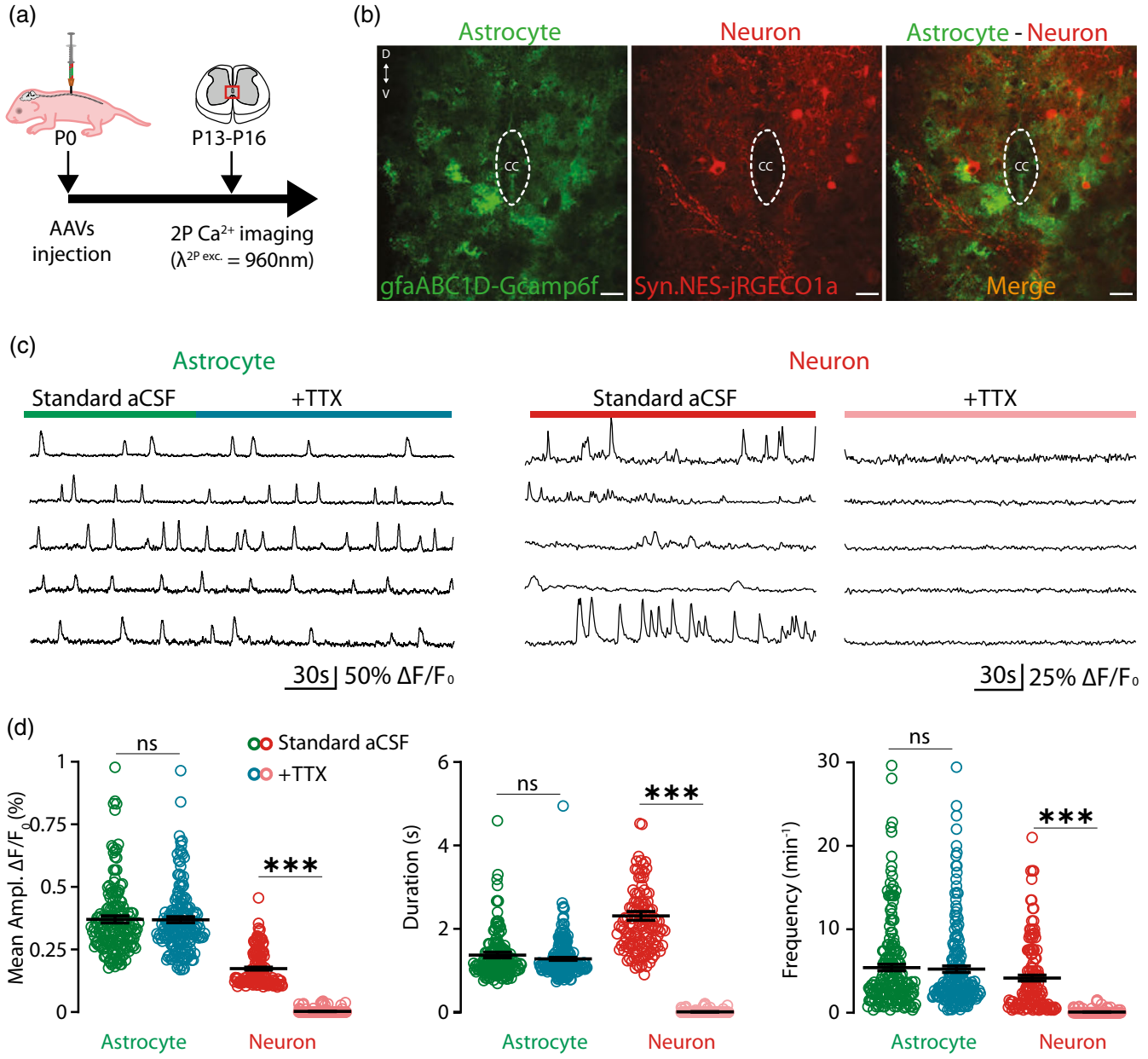

FIGURE 2 Simultaneous recording of neuronal and astrocytic signals by using two-photon Ca^{2+} imaging in lumbar slices. (a) Schematic representation of the experimental design. Intrathecal injections of AAV9-gfaABC1D-Gcamp6f and AAV9-Syn.NES-jRGECO1a were made at birth in wild-type mice. Two-photon Ca^{2+} imaging sessions on lumbar slices (L1–L2) were processed from P13–P16 mice. Red inset represents the imaging area. (b) Two-photon fluorescent images of Gcamp6f (astrocyte, left), jRGECO1a (neurons, middle) and merge signal (right) in the ventromedial part of a lumbar slice from a P16 mouse. CC means central canal. Scale bar is 40 µm. (c) Examples of astrocytic Gcamp6f Ca^{2+} transients ($\Delta F/F_0$) (left) and neuronal jRGECO1a Ca^{2+} transients (right) in presence or not of TTX. (d) Quantification of the mean amplitude (left), duration (middle) and frequency (right) of the astrocytic and neuronal Ca^{2+} transients in absence (green circles for astrocytes red circles for neurons) or in presence (blue circles for astrocytes, pink circles for neurons) of TTX ($n = 182$ astrocytic ROIs from 3 mice and $n = 141$ neuronal ROIs from 5 mice). Ns, no significance, $^{***}p < 0.001$ (two-tailed Wilcoxon test for (d)). Mean ± SEM. For detailed p values, see Source data file

3.4 | Kir4.1 channels are expressed in astrocytes from the spinal locomotor CPG region

We next investigated whether Kir4.1 channels are expressed in the spinal locomotor CPG. Using Hb9-eGFP mice which express GFP+ interneurons with intrinsic bursting properties (Tazerart et al., 2008; Ziskind-Conhaim et al., 2008), we found that ventromedial GFP+ interneurons were enwrapped by Kir4.1 labeling, which is diffusely expressed in the gray matter of the upper lumbar segments (Figure 5a). To confirm that Kir4.1 channels in the locomotor CPG area are exclusively expressed in glial cells with a highest expression in astrocytes, we used the *Aldh1L1-eGFP* astrocyte-specific reporter mice (Cahoy et al., 2008). We examined co-expression of *Aldh1L1-eGFP* with immunolabeling of Kir4.1 channels and neuronal marker NeuN in lumbar slices. We observed that 100% of the GFP+ astrocytes expressed Kir4.1 channels contrary to NeuN+ cells, which lacked Kir4.1 staining (Figure 5b,c).

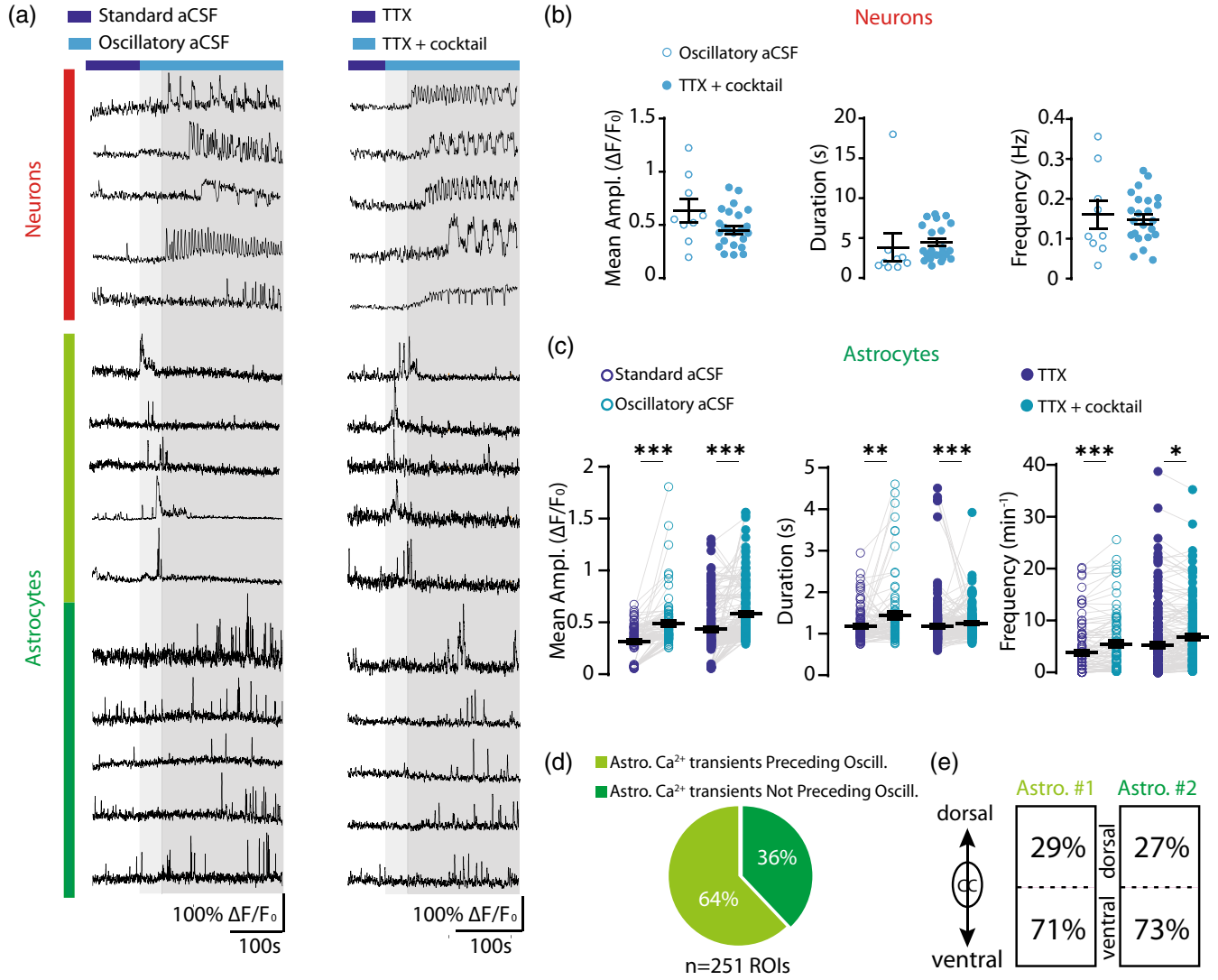

FIGURE 3 Increase in astrocytic Ca^{2+} transients is correlated to neuronal oscillations (a) Top: Examples of neuronal jRGECO1a Ca^{2+} transients ($\Delta F/F_0$) oscillating in response to oscillatory aCSF (K^+ rise and Ca^{2+} decrease) (left) or in response to the neuromodulator cocktail in presence of TTX (right). Middle and bottom: Examples of the increase of the astrocytic Gcamp6f Ca^{2+} signals ($\Delta F/F_0$) before (middle) or during (bottom) the neuronal oscillations (top) from the same field of view. (b) Quantification of the mean amplitude (left), duration and frequency (right) of the neuronal jRGECO1a Ca^{2+} transients in response to K^+ rise and Ca^{2+} decrease (empty blue circles) or in response to monoaminergic cocktail in presence of TTX (filled blue circles) ($n = 9$ and 24 dendritic ROIs from 2 and 3 mice in the ionic variation condition and in the TTX + cocktail condition, respectively). (c) Quantification of the mean amplitude (left), duration (middle) and frequency (right) of the astrocytic Gcamp6f Ca^{2+} signals in response to K^+ rise and Ca^{2+} decrease (empty light blue circles) or in response to monoaminergic cocktail in presence of TTX (filled light blue circles) ($n = 86$ and 165 astrocytic ROIs from 2 and 3 mice in the ionic variation condition and in the TTX + cocktail condition, respectively). (d) Proportion of astrocytic ROIs which display Ca^{2+} signals increase in amplitude and/or frequency before the onset of neuronal oscillations. (e) Proportion of astrocytic ROIs which display Ca^{2+} signals increase above (dorsal) or below (ventral) the central canal (CC) in response to oscillatory conditions (ionic variations and neuromodulator cocktail). Astro#1 and Astro#2 correspond to the astrocyte subtypes when Ca^{2+} transients precede or not the neuronal oscillations, respectively. *$p < 0.05$; **$p < 0.01$; ***$p < 0.001$ (two-tailed Wilcoxon paired test for (c)). Mean ± SEM. For detailed p values, see Source data file.

3.5 | The Ba^{2+}-sensitive inwardly rectifying K^+ (Kir4.1) current is crucial for maintaining neuronal oscillations and locomotor-like activity in the CPG

We next studied the role of Kir4.1 channels in the lumbar rhythmogenesis. We first induced rhythmic oscillations in the GFP+ ventromedial interneurons from Hb9-eGFP mice in response to $[K^+]_e/[Ca^{2+}]_e$ variations (Figures S2a, S3a) or bath perfusion of the neuromodulator cocktail in presence of TTX (Figures S2b, S3b). In both conditions, we noticed that before totally preventing the neuronal oscillations, the pharmacological blockade of Kir4.1 channels with Ba^{2+} (100 μM) progressively decreased the rhythmic bursting frequency accompanied with an increase in burst amplitude and duration in both conditions (Figure S2c). Then, Ba^{2+} progressively caused a

shift in the spiking pattern from bursting to tonic firing in ~70% of the TTX-sensitive neuronal oscillations (Figure S3c) or resulted in a cessation of bursting activity (~85%) of the TTX-insensitive neuronal oscillations (Figure S3d). We next confirmed the Ba^{2+} effect on preventing neuronal oscillations at a larger scale by two-photon Ca^{2+} imaging of cell populations. We observed a progressive loss of Ca^{2+} oscillations in the vast majority of neurons in response to Ba^{2+} in presence of the oscillatory aCSF (n = 25/28) or the neuromodulator cocktail (*n* = 7/9) (Figure S3e,f). Bath application of Ba^{2+} also induced a significant rise in amplitude of the astrocytic Ca^{2+} signal in both conditions (Figure S3g).

To confirm the functional role of the inwardly rectifying K^+ (Kir4.1) current in the integrated rhythmogenesis, we investigated the contribution of Kir4.1 in the locomotor rhythm-generating network by

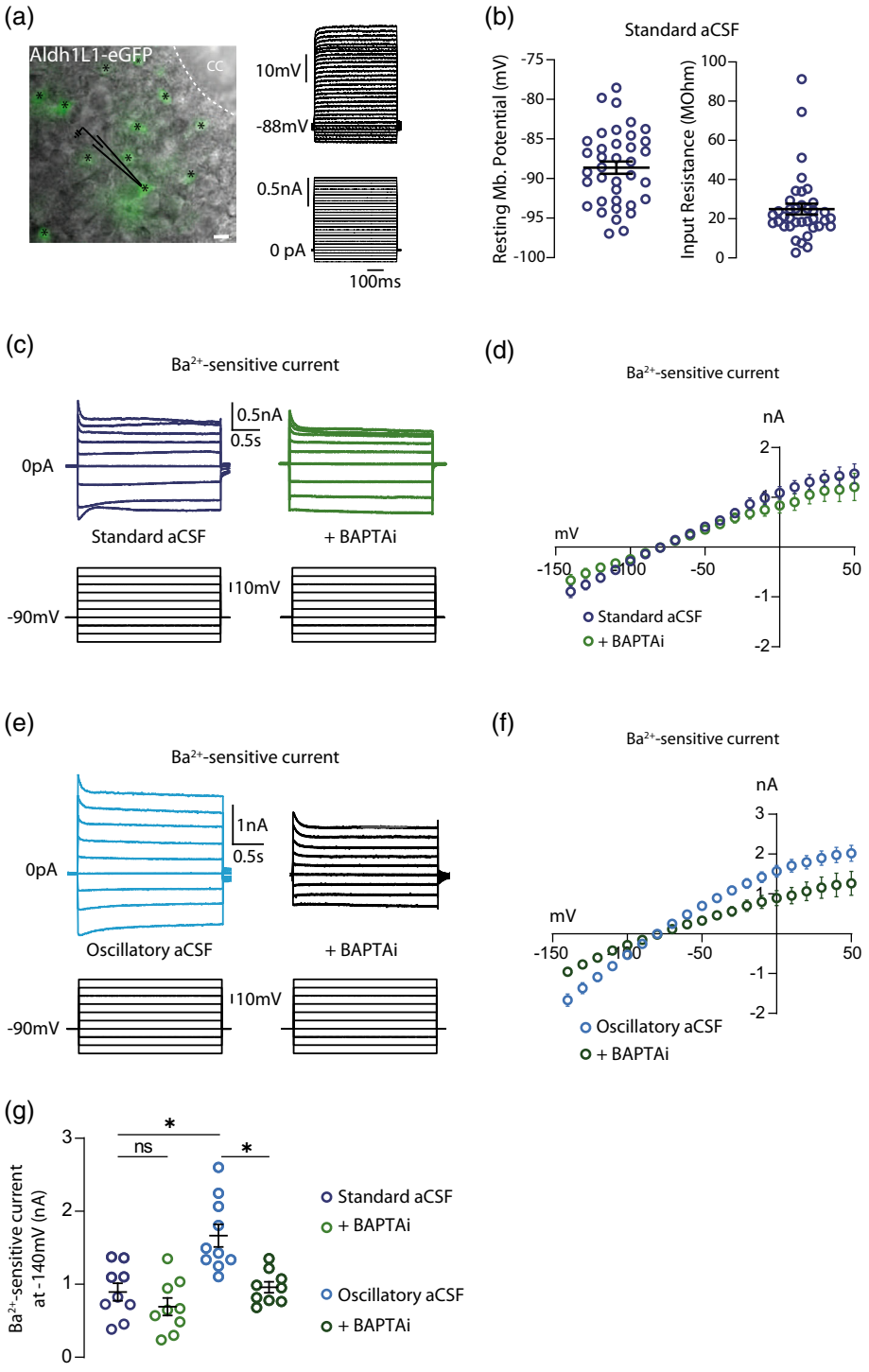

FIGURE 4 Legend on next page.

using ex vivo whole-mount spinal cords. Since rostral lumbar segments (L1–L2) have a more powerful rhythmogenic capacity than the caudal ones, we recorded locomotor-like activities from the contralateral L2 ventral roots (Figure S4a) in response to ionic variations (Figure S4b) or bath application of a neuromodulator cocktail composed of *N*-methyl-DL aspartate (NMA) and 5 hydroxytryptamine (5-HT) (Figure S4c). In both conditions, Ba^{2+} (100 μM) slowed down the locomotor rhythm by increasing the locomotor burst duration and decreasing the burst frequency without apparent effect on burst amplitude (Figure S4b–d). We also observed a decrease in the cross-correlogram coefficient in presence of Ba^{2+} related to a decreased rhythmic alternation (Figure S4e,f) confirming the role of Kir4.1 channels in modulating rhythmogenesis at the network level.

3.6 | Loss-of-function of Kir4.1 decreases the probability for ventromedial CPG interneurons to oscillate

Because the Ba^{2+} effect on neuronal oscillations cannot be exclusively attributed to Kir4.1 channels blockade, due its broad action on neuronal Kir channels (i.e., Kir2 family) (Li et al., 2013), we performed a targeted loss-of function of Kir4.1 channels by using a short hairpin RNAs (shRNAs) to evaluate more specifically the Kir4.1 contribution to spinal rhythmicity. We injected intrathecally at birth at T13–L1 level an AAV9 virus encoding the Kir4.1-shRNA with a eGFP reporter (Figure 6a,b). The viral transfection led to a decrease of ∼40% in Kir4.1 membrane protein expression in the lumbar spinal cord (Figure 6c). Concomitantly, a strong expression of eGFP in the ventromedial part of the spinal cord was observed from T1 to L5-S1 (Figure 6d, Figure S5). We first examined the effect of Kir4.1-shRNA on glial and neuronal electrophysiological properties. In the virally transfected GFP+ astrocytes (Figure S6a,b), we observed in whole-cell configuration a more depolarized RMP (Figure S6c), a higher input resistance (Figure S6c), a marked change in the current–voltage (*I–V*) relationship and a reduced Ba^{2+}-sensitive current in mice transduced with Kir4.1-ShRNA compared to Ctrl-ShRNA mice (Figure S6d–i). We also observed that the RMPs of ventromedial interneurons surrounded by the virally transfected GFP+ astrocytes (Figure 6e) from mice transduced with Kir4.1-ShRNA were overall more depolarized than the RMPs of interneurons from mice infected with Ctrl-ShRNA (Figure 6e,f), suggesting that knockdown of Kir4.1 in astrocytes had a widespread impact on the excitability of neighboring neurons.

We then tested the ability of the ventromedial interneurons to oscillate after the viral transfection of the spinal cord. We found a significant lower proportion of rhythmic bursting in ventromedial interneurons surrounded by GFP+ astrocytes in mice transduced with Kir4.1-ShRNA compared to Ctrl-ShRNA in response to both ionic variations (∼24% vs. 80%) (Figure 6g,i) or bath perfusion of the neuromodulator cocktail in presence of TTX (∼ 23% vs. 75%) (Figure 6h,j). Interestingly, we also performed two-photon Ca^{2+} imaging in lumbar slices with Rhod-2AM loading (Figure S7a) (Carlsen et al., 2021; Otsu et al., 2015) from Kir4.1 ShRNA transgenic mice, which strengthened our results obtained with the pharmacological (Ba^{2+}) approach (Figure S3g). We show that astrocytic Ca^{2+} transients recorded in oscillatory conditions (Figure S7b,c) were significantly increased in Kir4.1-ShRNA mice compared to Ctrl-ShRNA mice (Figure S7d,e). We also demonstrate that Ba^{2+} had no additional effect on astrocytic Ca^{2+} transients in Kir4.1-ShRNA mice, in contrast to its effect found in Ctrl-ShRNA mice (Figure S7d,e). This suggests that the Ba^{2+} effect on astrocytic Ca^{2+} transients in control mice results from the inhibition of astrocytic Kir4.1 channels. Altogether, these data demonstrate the pivotal role of astrocytic Kir4.1 channels in the oscillatory pattern of ventromedial interneurons from the CPG.

3.7 | Loss-of-function of Kir4.1 slows down the in vivo locomotor pattern and decreases the locomotor performances

We then tested whether the knockdown of Kir4.1 in the spinal cord has a functional impact on the locomotor behaviors. We thus injected intrathecally at birth an AAV9 encoding either the Kir4.1-shRNA or the Ctrl-shRNA. From 12 to 18 days after the viral injection, we

FIGURE 4 Spinal astrocytes display a Ba^{2+}-sensitive Kir4.1 current modulated by intracellular Ca^{2+}. (a) Left: DIC image of a lumbar slice from a P8 *Aldh1L1-eGFP* mouse superimposed with the fluorescent GFP signal. The black stars indicate the GFP+ astrocytes. The recording glass pipette is represented in black. Right: Representative membrane potentials (top) of the targeted GFP+ astrocyte (left image) in response to incremental current pulses (500 ms, Δ = 50 pA). (b) Resting membrane potential (RMP) (left) and input resistance (right) of lumbar GFP+ astrocytes recorded in standard aCSF ($[K^+]_e$ 3 mM and $[Ca^{2+}]_e$ 1.2 mM) ($n = 37$ astrocytes from $n = 20$ mice). (c) Superimposed Ba^{2+}-sensitive currents (top) of two GFP+ astrocytes clamped at the RMP in response to incremental voltages pulses (bottom, 2.5 s, −140 to −30 mV, Δ = 10 mV) without (blue traces) or with (green traces) intracellular perfusion of BAPTA (30 mM) in standard aCSF. (d) The averaged I/V relationship of the Ba^{2+}-sensitive currents of GFP+ astrocytes without (blue circles) ($n = 9$ astrocytes from 5 mice) or with (green circles) ($n = 9$ astrocytes from 5 mice) intracellular BAPTA perfusion in standard aCSF. (e) Superimposed Ba^{2+}-sensitive currents (top) of two GFP+ astrocytes clamped at the RMP in response to incremental voltages pulses (2.5 s, −140 to −30 mV, Δ = 10 mV) without (light blue traces) or with (dark green traces) intracellular perfusion of BAPTA (30 mM) in oscillatory aCSF ($[K^+]_e$ 6 mM and $[Ca^{2+}]_e$ 0.9 mM). (f) The averaged *I/V* curves of the Ba^{2+}-sensitive currents of GFP+ astrocytes without (light blue circles) ($n = 10$ astrocytes from 5 mice) or with (dark green circles) ($n = 9$ astrocytes from 5 mice) intracellular BAPTA perfusion in oscillatory aCSF. (g) Average effect of oscillatory aCSF and intracellular perfusion of BAPTA on the peak amplitude of the astrocytic Kir4.1 current at −140 mV compared to standard aCSF ($n = 8$ and 7 astrocytes from 3 and 4 mice for control and BAPTAi, respectively). Ns, no significance, $^*p < 0.05$ (Kruskal–Wallis one-way ANOVA test with Dunn's post hoc test for (g)). Mean ± SEM. For detailed *p* values, see Source data file.

performed a set of behavioral locomotor tests on freely moving mice (Figure 7a). We first used footprint analysis to evaluate the locomotor pattern (Figure 7b). Mice transduced with Kir4.1-shRNA displayed an increase in both swing and stand phases compared to Ctrl-ShRNA mice (Figure 7c,d) related to a slower speed of locomotion and a decrease in regularity index without any modification of the base of

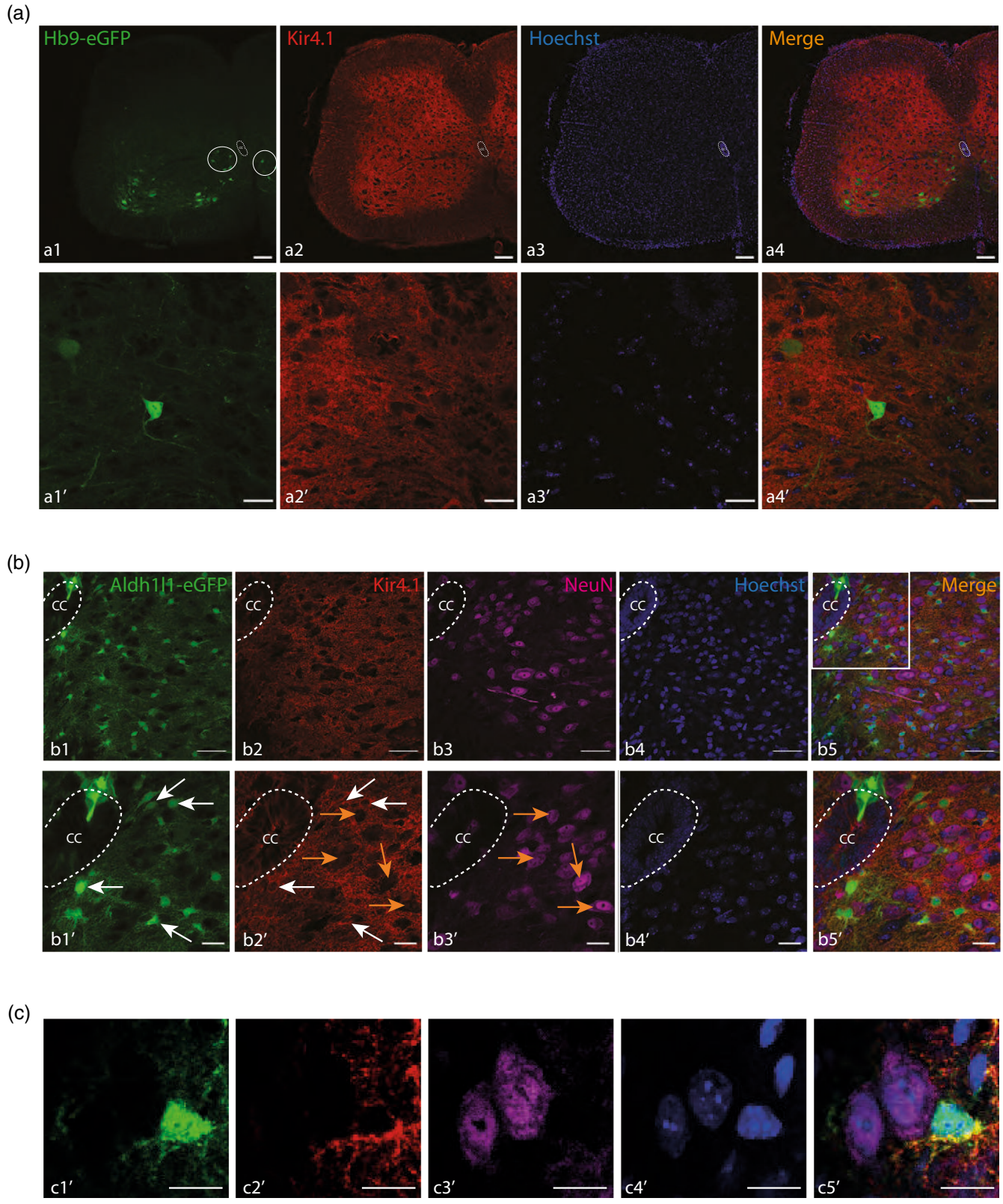

FIGURE 5 Legend on next page.

support (Figure 7d). We next tested whether Kir4.1 channels also modulate locomotor behaviors in more challenging tasks. We thus assayed motor coordination using the rotarod and swimming forced test without practice sessions to avoid any compensatory learning mechanisms. Consistently, mice transduced with Kir4.1-shRNA failed to adapt to accelerated speed (Figure 7e) and displayed a lower swimming performance (Figure 7f). Kir4.1 channels contribute to the maintenance of the soma size of large α-motoneurons and peak strength in adult mice (Kelley et al., 2018). We demonstrated that the lowered locomotor performances from Kir4.1-ShRNA mice do not result from changes in motoneuronal morphological features. Indeed, we did not observe any modification of the motoneuronal soma size in mice transduced with Kir4.1-ShRNA compared to Ctrl-ShRNA mice (Figure S8). In sum, the Kir4.1-mediated inwardly rectifying K^+ current appears to play a key role for locomotor coordination and the maintenance of the locomotor pattern in freely moving mice.

4 | DISCUSSION

This study demonstrates that astrocytic regulation of extracellular K^+ plays a critical role in maintenance of neuronal rhythmogenesis in the spinal cord motor circuitry. We report that spinal astrocytes from neonatal mice display Ca^{2+} signals before and during rhythmic neuronal oscillations. Inhibiting astrocytic Ca^{2+} transients with BAPTA decreases the Ba^{2+}-sensitive inwardly rectifying K^+ current underlying K^+ uptake. The Kir4.1 channels mediating the K^+ current are expressed in astrocytes enwrapping the ventromedial interneurons from the locomotor CPG. We also demonstrated that knockdown of Kir4.1 decreases the ability of the ventromedial interneurons to oscillate. This perturbation results in an alteration of the locomotor pattern and in lower locomotor performances in challenging tasks.

4.1 | Functional coupling of astrocytic Ca^{2+} signals and neuronal oscillations

Recent studies have highlighted unexpected contribution of astrocytic Ca^{2+} signals in regulating rhythmic behaviors including respiration (Sheikhbahaei et al., 2018), mastication (Morquette et al., 2015) and locomotion (Broadhead & Miles, 2020). However, it is still incompletely understood whether the increased astrocytic Ca^{2+} transient is a prerequisite or a consequence of neuronal oscillations. Here, we reveal that ventromedial astrocytes depolarize and display an increase in Ca^{2+} signals both before and in response to ions and neuromodulator changes related to neuronal oscillations. Our two-photon Ca^{2+} imaging data reveal a functional coupling between spinal cord astrocytes and CPG interneurons. The simultaneous imaging of neuronal and astrocytic activity led to the characterization of distinct subsets of active astrocytes in the spinal CPG area. In one subset, the response precedes neuronal oscillation. This active role of astrocytes in rhythmicity has been suggested in the trigeminal sensorimotor circuit (Morquette et al., 2015) or in cortical areas where the increase in astrocytic Ca^{2+} events precedes the switch to the slow-oscillation state (Poskanzer & Yuste, 2016). In another group, the responses are concomitant to neuronal bursting. In line with this, in Drosophila astrocyte Ca^{2+} transients are driven by rhythmic firing of the octopaminergic neurons (Ma et al., 2016). A recent study also demonstrated such a dynamics in fish radial astroglia (analogs of the mammalian astrocyte), where the noradrenergic neuronal activity precedes the Ca^{2+} wave observed in radial astroglia (Mu et al., 2019). However, we cannot totally rule out that one astrocyte may belong to both groups. Altogether, our data highlight a bi-directional coupling between astrocytic Ca^{2+} signal and neuronal oscillations.

4.2 | The Ca^{2+}-dependent K^+ uptake in spinal astrocytes

Astrocytic Ca^{2+} transients are often associated to gliotransmission (Araque et al., 2014). Here we propose that an alternative mechanism to the classical gliotransmission operates for spinal rhythmogenesis. Previous works demonstrated that GPCR-mediated Ca^{2+} signaling in astrocytes is linked to an increase of K^+ uptake in hippocampus (Wang, Smith, et al., 2012) and cerebellum (Wang, Xu, et al., 2012). This astrocytic Ca^{2+} transients stimulate the Na^+, K^+ ATPase pump resulting in a transient decrease in $[K^+]_e$. In our study, we provide for

FIGURE 5 Spinal astrocytes express Kir4.1 channels enwrapping the pacemaker interneurons. (a) Top: Representative confocal images of the endogenous neuronal GFP signal (a1) and the immunofluorescent labelling of the Kir4.1 channels (a2) from a lumbar slice of a P12 Hb9-eGFP mouse. Note the nuclei are labeled in blue with Hoechst (a3) and the merge signal is shown in a4. White circles indicate the targeted bursting GFP+ interneurons. CC stands for central canal. Scale bar, 100 µm. Bottom: High magnification images of the upper ventromedial part of the lumbar slice from one Hb9-eGFP mouse showing the Kir4.1 channels (a2') enwrapping the GFP signal of a pacemaker interneuron (a1') co-stained with Hoechst (a3'). Merge signal is shown in a4'. Scale bar, 20 µm. (b) Top: Representative confocal images of the endogenous astrocytic GFP signal (b1), the immunofluorescent labelling of the Kir4.1 channels (b2) and the neurons immuno-stained with NeuN (b3) from a lumbar slice of a P8 *Aldh1L1-eGFP* mouse. The nuclei are labeled in blue with Hoechst (b4) and the merge signal is shown in (b5). Scale bar, 50 µm. CC for central canal. Bottom: High magnification images of the upper white inset (b5) showing the GFP+ astrocytes (b1') expressing the Kir4.1 channels (white arrows) (b2'). The Kir4.1 signal does not merge with NeuN signal (orange arrows) (b3'). All nuclei cells are stained with Hoechst signal (b4'). Merge signal is shown in b5'. Scale bars, 20 µm. (c) High magnification (63×) images showing one ventromedial GFP+ astrocyte (c1') expressing Kir4.1 (c2') surrounding two ventromedial interneurons (NeuN+) which are not labeled for Kir4.1 (c3'). All nuclei cells are stained with Hoechst signal (c4'). Merge signal is shown in c5'. Scale bars, 10 µm

the first time evidence that a blockade of the Ca^{2+} transients from ventromedial lumbar astrocytes significantly reduces the Ba^{2+}-sensitive current mediated by Kir4.1. This result is in line with observations showing that menthol-induced Ca^{2+} transients in astrocytes increases the Ba^{2+}-sensitive Kir4.1 current from a U251 cell line (Ratto et al., 2020). One likely mechanism underlying the Ca^{2+}-dependent modulation of K^+

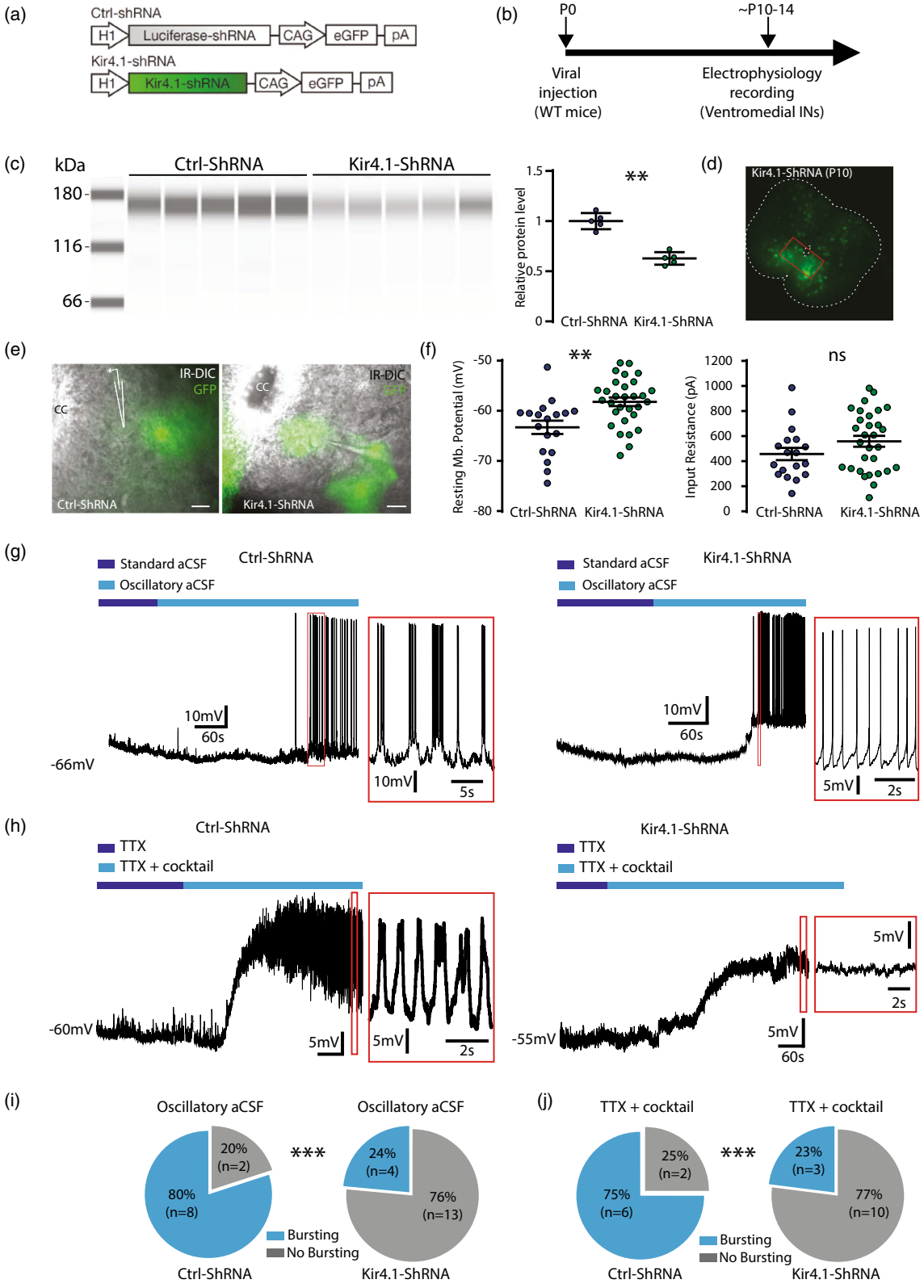

FIGURE 6 Legend on next page.

uptake may rely on activity-dependent pH shift, since pH alkalinization may be induced in astrocytes by increased Ca^{2+} transients following neuronal oscillations (Grichtchenko & Chesler, 1996), and such Ca^{2+}-dependent alkaline pH-shift in astrocytes is known to increase Ba^{2+}-sensitive Kir4.1 currents (Xu et al., 2000). Because (i) the locomotor-like activity is associated with $[K^+]_e$ homeostasis (Brocard et al., 2013), and (ii) the astrocytic K^+ uptake is activated by intracellular Ca^{2+} transients (Wang, Smith, et al., 2012), we assume that the Ca^{2+} dependent astrocytic K^+ homeostasis plays a key role in the spinal rhythmicity.

4.3 | Astrocytic-dependent K^+ regulation of the spinal rhythmogenesis

The maintenance of K^+ homeostasis by astrocytes is crucial in modulating neuronal excitability (Dallérac et al., 2013; Neprasova et al., 2007). However, whether spinal astrocytes may exert a "ionostatic control" of neuronal bursting, as suggested by Ding et al., 2016, is still unclear. Here, we evaluated the consequence of blocking the astrocytic inwardly rectifying K^+ (Kir4.1) channels on neuronal oscillations in the locomotor CPG. Blocking the Kir4.1-mediated astrocytic K^+ uptake with Ba^{2+} (100 μM) (Cui et al., 2018; Djukic et al., 2007; Ransom & Sontheimer, 1995) decreases the frequency of neuronal oscillations until progressively preventing them. In line with this effect, injection of Kir4.1-ShRNA resulting in the decrease in Kir4.1 astrocytic membrane expression also significantly reduces the probability of driving neuronal oscillations. These results highlight the key role of astrocytic K^+ uptake in maintaining the neuronal oscillatory pattern. Although the astrocytic Kir4.1 channels are not homogeneously expressed among and within brain structures (Higashi et al., 2001), we showed a strong Kir4.1 expression in astrocytes enwrapping the ventromedial bursting interneurons and lamina IX motoneurons. This strategic distribution of Kir4.1 channels surrounding the bursting spinal neurons may be viewed as a powerful mechanism to rapidly modulate network rhythmicity. Moreover, since glutamate tunes the CPG network by exerting a speed control of locomotor-like activity (Talpalar et al., 2013) and that $[K^+]_e$ provides the driving force for glutamate uptake (Nwaobi et al., 2016; Verkhratsky & Nedergaard, 2018) the effective K^+ uptake from the extracellular space through Kir4.1 is thus crucial for tuning the neuron oscillations. In line with this, previous works highlighted the importance of $[K^+]_e$ for rhythmogenesis in hippocampal (Jensen et al., 1994), the increase in $[K^+]_e$ induced by neuromodulators may promote the shift between neuronal oscillatory states in cortical slices electrically silenced by TTX (Ding et al., 2016). A computational work also demonstrated that extracellular K^+ dynamics can cause transition between fast tonic spiking and slow bursting in neocortical networks (Frohlich et al., 2006) in the same range than the spinal locomotor network. Also, we cannot rule out the contribution of the gap junction-coupled astrocytic networks diffusing K^+ to non-active areas (Mazaud et al., 2021). Several studies indeed showed in the trigeminal sensory network (Condamine et al., 2018) or hippocampal circuit (Chever et al., 2016) that astrocytic gap junctions promote neuronal bursting in an activity-dependent manner by favoring the recruitment of neuronal assemblies. Further experiments will be necessary to identify the connexins working in conjunction with Kir4.1 for modulating the spinal locomotor rhythm.

4.4 | The ventromedial astrocytes regulate the locomotor pattern in vivo

A dense literature pointed out that during locomotion, mice display enhanced Ca^{2+} signals in astrocytes of the cerebellum (Nimmerjahn et al., 2009; Paukert et al., 2014), visual cortex (Paukert et al., 2014), or somatosensory cortex (Bojarskaite et al., 2020; Dombeck et al., 2007). On the other hand, silencing astrocyte Ca^{2+} activity in brainstem with optogenetics or chemogenetics can modulate the rhythmic respiratory behavior (Gourine et al., 2010; Sheikhbahaei et al., 2018). In this study, we used genetic tools with ShRNA to knockdowns Kir4.1 in the locomotor CPG and demonstrate that the astrocytic regulation of K^+ homeostasis plays a key role in controlling the locomotor speed and challenging locomotor tasks in vivo. Mice transduced with Kir4.1-ShRNA showed striking locomotor deficits compared to Ctrl-ShRNA mice. Kir4.1 had been reported to contribute to the maintenance of the soma size of large α-motoneurons

FIGURE 6 Targeted decrease in Kir4.1 channels reduces the occurrence of neuronal oscillations. (a) Schematics of the AAV vector engineered to overexpress shRNA or dominant-negative Kir4.1. H1, human H1 promoter; CAG, CMV early enhancer/chicken *Actb* promoter. (b) Schematic representation of the experimental design. WT for wild-type, INs for interneurons and P for postnatal day. (c) Left: Kir4.1 pseudo-gel images from Capillary Western Blot of lumbar segments from P14 intrathecally injected at birth with an adeno-associated virus (AAV9) encoding either a control shRNA ($n = 5$ mice) or a Kir4.1-targeting shRNA ($n = 5$ mice). One mouse per column. Right: group mean quantification of the ~168 kDa band normalized to luciferase-injected controls. (d) Representative image of GFP in lumbar slices from P10 mice after intrathecal injection at birth of an adeno-associated virus (AAV9) encoding a Kir4.1-targeting shRNA (Kir4.1-ShRNA). (e) DIC image of the ventromedial part of a lumbar slice and the corresponding one-photon GFP signal (right) of a P10 mouse injected with AAV9-Ctrl-ShRNA (left) or AAV9-Kir4.1-ShRNA (right). CC means central canal. Scale bars, 20 μm. (f) Quantification of the mean RMP (left) and input resistance (right) of ventromedial interneurons from wild-type mice injected with AAV9 encoding for Ctrl-ShRNA (left, $n = 18$ neurons from 4 mice) or Kir4.1-ShRNA (right, $n = 30$ neurons from 5 mice). (g-h) Representative voltage traces of one interneuron of a mouse injected with AAV9-Ctrl-ShRNA (left) or AAV9-Kir4.1-ShRNA (right) in response to ionic changes (g) or in response to the neuromodulator cocktail in presence of TTX (h). (i,j) Proportion of oscillatory interneurons (blue) or not (gray) from mice injected at birth with an AAV9 encoding either a Luciferase shRNA (Ctrl-ShRNA, $n = 4$ mice) (left) or a Kir4.1-targeting shRNA (Kir4.1-ShRNA, $n = 7$ mice) (right) in presence of high $[K^+]_e$ and low $[Ca^{2+}]_e$ (i) or in presence of the neuromodulator cocktail + TTX (j). ns, no significance, $^{**}p < 0.01$; $^{***}p < 0.001$ (two-tailed Mann–Whitney test for (c) and (f), two-tailed Fisher test for (i) and (j)). Mean ± SEM. For detailed *p* values, see Source data file

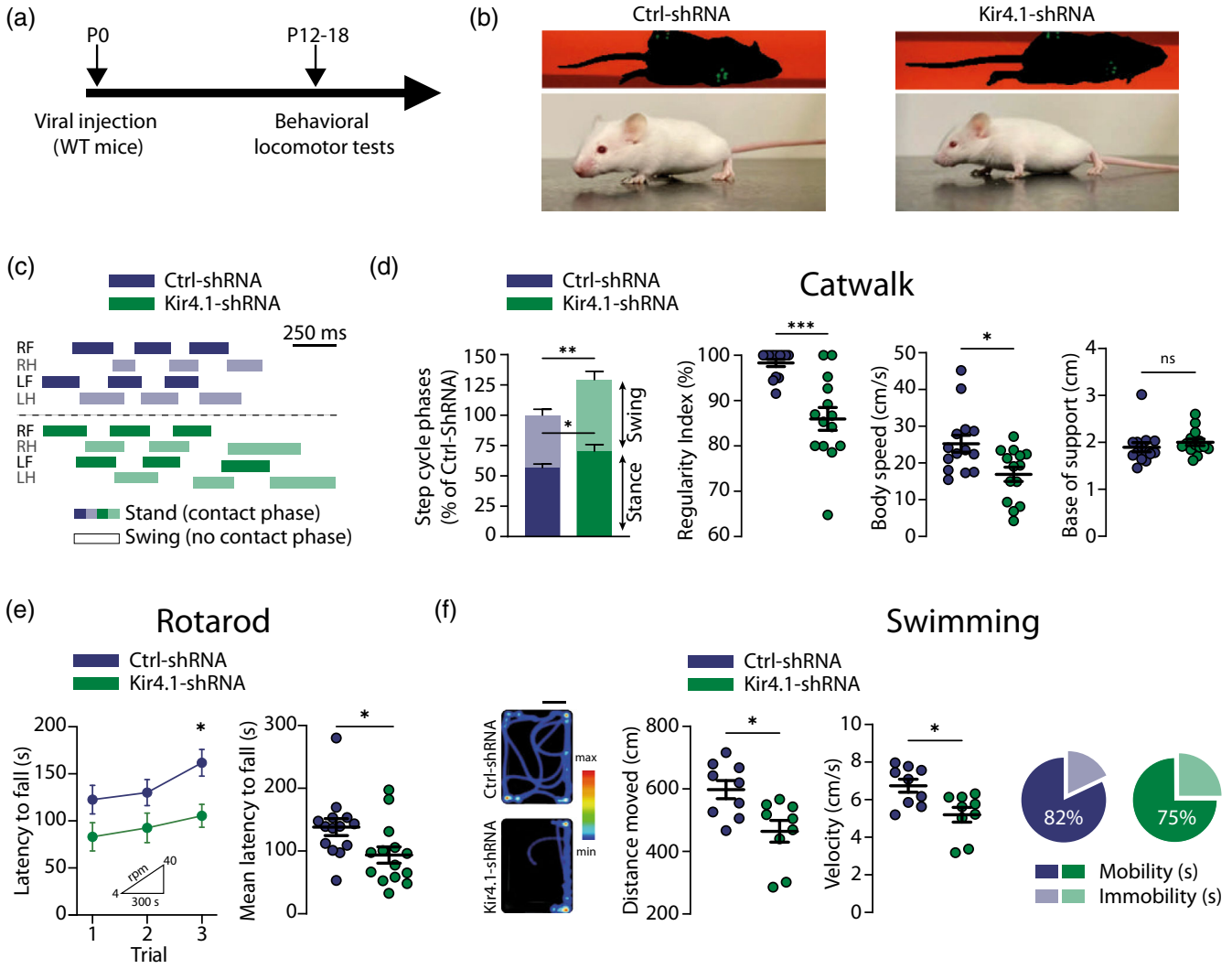

FIGURE 7 Astrocytic Kir4.1 channels influence the locomotor behavior. (a) Schematic representation of the experimental design. WT for wild-type and P for postnatal day. (b) Top: Bottom view of P18 mice injected at birth with AAV9 encoding either for the Ctrl-ShRNA (left) or the Kir4.1-ShRNA (right) freely walking on a glass platform (Catwalk). Bottom: Side view of the same P18 mice. (c) Representative footfall diagrams during CatWalk locomotion of a Ctrl-ShRNA P18 mouse (blue, top) or Kir4.1-ShRNA P18 mice (green, bottom). The stance phase is indicated by horizontal bars and the swing phase by open spaces. RF for Right Forelimb, RH for Right Hindlimb, LF for Left Forelimb, LH for Left Hindlimb. (d) Comparative quantification of the normalized step cycle phases (stance, swing) (left), regularity index (middle left), body speed (middle right) and hind limb base of support (right) between Ctrl-ShRNA mice (blue, $n = 14$ mice) and Kir4.1-ShRNA mice (green, $n = 14$ mice). Each circle represents an individual mouse. (e) Latency to fall from a rod rotating at accelerated speed (4–40 rpm) during 300 s of wild-type mice transduced either with the Ctrl-ShRNA (blue, $n = 14$ mice) or with Kir4.1-ShRNA (green, $n = 14$ mice). (f) Left: Heatmaps illustrate the swimming activity of two wild-type mice transduced either with the Ctrl-ShRNA (top) or with the Kir4.1-shRNA (bottom). Scale bar, 10 cm. Middle: Comparison of the mean swimming distance (middle left) and the mean velocity (middle right) between Ctrl-shRNA (blue, $n = 9$ mice) and Kir4.1-shRNA (green, $n = 9$ mice) mice. Each circle represents one individual mouse. Right: Percentage of mobility and immobility for Ctrl-shRNA mice (blue, $n = 9$ mice) and Kir4.1-shRNA mice (green, $n = 9$ mice) during the swimming forced test. ns, no significance, $^{*}p < 0.05$; $^{**}p < 0.01$; $^{***}p < 0.001$ (Mann–Whitney test for (d), (e) right and (f), Two-way ANOVA with Sidak's multiple comparisons test for (e) left). Mean ± SEM. For detailed p values, see Source data file

and peak strength in adult mice (Kelley et al., 2018). We demonstrated that the lowered locomotor performances from Kir4.1-ShRNA mice do not result from changes in motoneuronal morphological features. Indeed, we did not observe any modification of the motoneuronal soma size in mice transduced with Kir4.1-ShRNA compared to Ctrl-ShRNA mice. Tong et al., 2014 observed that the Kir4.1 expression decrease in the striatal network of a mouse model of Huntington disease, results in altered locomotor pattern (Tong et al., 2014). We did not observe any Kir4.1-ShRNA expression in brain or brainstem structures involved in the locomotor control. This result is in line with the restricted diffusion to the thoraco-lumbar segments of the AAV9-ShRNA injected intrathecally at birth in the lumbar segments (Bos et al., 2021). Thus we assume that the behavioral consequence of Kir4.1 knockdown on locomotor performances is due to Kir4.1 decrease in the spinal locomotor networks.

Overall this study defines the contours of a new concept for the spinal locomotor CPG. We propose that the astrocytic Ca^{2+} transients which occurs during the neuronal oscillations likely maintains extracellular K^+ homeostasis, which in turn adjusts the locomotor pattern. Further studies will be needed to decipher the importance for spinal rhythmicity of the astrocytic network mediating K^+ buffering in the locomotor CPG.

AUTHOR CONTRIBUTIONS

Tony Barbay, Emilie Pecchi, and Rémi Bos: Research design; Tony Barbay, Emilie Pecchi, Nathalie Rouach, and Rémi Bos: Methodology; Tony Barbay, Emilie Pecchi, Myriam Ducrocq, and Rémi Bos: Investigation and data analysis; Tony Barbay and Rémi Bos: Figures design; Rémi Bos: Writing; Rémi Bos and Frédéric Brocard: Funding Acquisition; Rémi Bos: Supervision.

ACKNOWLEDGMENTS

We thank I. Vanzetta, P. Weber and S. Roux for their technical advices in imaging sessions, A. Duhoux for animal care, C. Brocard for genotyping and J. Verneuil for providing the Matlab script. We also gratefully acknowledge E. Gascon, F. Jaouen, C. Lepolard and A. Borges-Correia from Neuro-Vir platform of the Neuro-Bio-Tools facility (Institut de Neurosciences de la Timone, UMR 7289, Marseille, France) for their advices, support and assistance in the design and production of vectors used in this work. We also thank G. Rougon for her critical insights on the manuscript.

FUNDING INFORMATION

This work was mainly funded by the CNRS and "Fonds d'Investissement de l'INT jeunes chercheuses, jeunes chercheurs" (FI_INT_JCJC_2019) (to Rémi Bos), by the French Ministry of Higher Education, Research and Innovation (PhD fellowship to Tony Barbay) and for a minor part by the Agence National de la Recherche Scientifique (CalpaSCI, ANR-16-CE16-0004) (to Frédéric Brocard).

CONFLICT OF INTEREST

The authors declare no conflict of interest.

DATA AVAILABILITY STATEMENT

The data that support the findings of this study are openly available in (remibos/Source-data-file) at https://github.com/remibos/Source-data-file.git. Code/software available at https://github.com/remibos/Analysis_2P.git.

ORCID

Nathalie Rouach https://orcid.org/0000-0002-5574-888X
Rémi Bos https://orcid.org/0000-0003-2639-3271

REFERENCES

Araque, A., Carmignoto, G., Haydon, P. G., Oliet, S. H. R., Robitaille, R., & Volterra, A. (2014). Gliotransmitters travel in time and space. *Neuron*, *81*(4), 728–739. https://doi.org/10.1016/j.neuron.2014.02.007

Bellot-Saez, A., Cohen, G., van Schaik, A., Ooi, L., Morley, J. W., & Buskila, Y. (2018). Astrocytic modulation of cortical oscillations. *Scientific Reports*, *8*(1), 11565. https://doi.org/10.1038/s41598-018-30003-w

Ben Haim, L., Carrillo-de Sauvage, M. A., Ceyzeriat, K., & Escartin, C. (2015). Elusive roles for reactive astrocytes in neurodegenerative diseases. *Frontiers in Cellular Neuroscience*, *9*, 278. https://doi.org/10.3389/fncel.2015.00278

Bojarskaite, L., Bjornstad, D. M., Pettersen, K. H., Cunen, C., Hermansen, G. H., Abjorsbraten, K. S., Chambers, A. R., Sprengel, R., Vervaeke, K., Tang, W., Enger, R., & Nagelhus, E. A. (2020). Astrocytic Ca(2+) signaling is reduced during sleep and is involved in the regulation of slow wave sleep. *Nature Communications*, *11*(1), 3240. https://doi.org/10.1038/s41467-020-17062-2

Bos, R., Drouillas, B., Bouhadfane, M., Pecchi, E., Trouplin, V., Korogod, S. M., & Brocard, F. (2021). Trpm5 channels encode bistability of spinal motoneurons and ensure motor control of hindlimbs in mice. *Nature Communications*, *12*(1), 6815. https://doi.org/10.1038/s41467-021-27113-x

Bos, R., Harris-Warrick, R. M., Brocard, C., Demianenko, L. E., Manuel, M., Zytnicki, D., Korogod, S. M., & Brocard, F. (2018). Kv1.2 channels promote nonlinear spiking Motoneurons for powering up locomotion. *Cell Reports*, *22*(12), 3315–3327. https://doi.org/10.1016/j.celrep.2018.02.093

Bracci, E. B. M., & Nistri, A. (1998). Extracellular K+ induces locomotor-like patterns in the rat spinal cord In vitro: Comparison with NMDA or 5-HT induced activity. *Journal of Neurophysiology*, *79*(5), 2643–2652. https://doi.org/10.1152/jn.1998.79.5.2643

Broadhead, M. J., & Miles, G. B. (2020). Bi-directional communication between neurons and astrocytes modulates spinal motor circuits. *Frontiers in Cellular Neuroscience*, *14*, 30. https://doi.org/10.3389/fncel.2020.00030

Brocard, F., Shevtsova, N. A., Bouhadfane, M., Tazerart, S., Heinemann, U., Rybak, I. A., & Vinay, L. (2013). Activity-dependent changes in extracellular Ca2+ and K+ reveal pacemakers in the spinal locomotor-related network. *Neuron*, *77*(6), 1047–1054. https://doi.org/10.1016/j.neuron.2013.01.026

Brocard, F., Tazerart, S., & Vinay, L. (2010). Do pacemakers drive the central pattern generator for locomotion in mammals? *The Neuroscientist*, *16*(2), 139–155. https://doi.org/10.1177/1073858409346339

Cahoy, J. D., Emery, B., Kaushal, A., Foo, L. C., Zamanian, J. L., Christopherson, K. S., Xing, Y., Lubisher, J. L., Krieg, P. A., Krupenko, S. A., Thompson, W. J., & Barres, B. A. (2008). A transcriptome database for astrocytes, neurons, and oligodendrocytes: A new resource for understanding brain development and function. *Journal of Neuroscience*, *28*(1), 264–278. https://doi.org/10.1523/JNEUROSCI.4178-07.2008

Carlsen, E. M. M., Falk, S., Skupio, U., Robin, L., Pagano Zottola, A. C., Marsicano, G., & Perrier, J. F. (2021). Spinal astroglial cannabinoid receptors control pathological tremor. *Nature Neuroscience*, *24*(5), 658–666. https://doi.org/10.1038/s41593-021-00818-4

Carlsen, E. M. M., & Perrier, J.-F. (2014). Purines released from astrocytes inhibit excitatory synaptic transmission in the ventral horn of the spinal cord. *Frontiers in Neural Circuits*, *8*, 60. https://doi.org/10.3389/fncir.2014.00060

Chever, O., Dossi, E., Pannasch, U., Derangeon, M., & Rouach, N. (2016). Astroglial networks promote neuronal coordination. *Science Signaling*, *9*(410), ra6. https://doi.org/10.1126/scisignal.aad3066

Condamine, S., Lavoie, R., Verdier, D., & Kolta, A. (2018). Functional rhythmogenic domains defined by astrocytic networks in the trigeminal main sensory nucleus. *Glia*, *66*(2), 311–326. https://doi.org/10.1002/glia.23244

Cui, Y., Yang, Y., Ni, Z., Dong, Y., Cai, G., Foncelle, A., Shuangshuang, M., Sang, K., Tang, S., Li, Y., Shen, Y., Berry, H., Wu, S., & Hu, H. (2018). Astroglial Kir4.1 in the lateral habenula drives neuronal bursts in depression. *Nature*, *554*(7692), 323–327. https://doi.org/10.1038/nature25752

Dallérac, G., Chever, O., & Rouach, N. (2013). How do astrocytes shape synaptic transmission? Insights from electrophysiology. *Frontiers in Cellular Neuroscience*, *7*, 159. https://doi.org/10.3389/fncel.2013.00159

Ding, F., O'Donnell, J., Xu, Q., Kang, N., Goldman, N., & Nedergaard, M. (2016). Changes in the composition of brain interstitial ions control the sleep-wake cycle. *Science*, *352*(6285), 550–555. https://doi.org/10.1126/science.aad4821

Djukic, B., Casper, K. B., Philpot, B. D., Chin, L.-S., & McCarthy, K. D. (2007). Conditional Knock-out of Kir4.1 leads to glial membrane depolarization, inhibition of potassium and glutamate uptake, and enhanced short-term synaptic potentiation. *Journal of Neuroscience*, *27*(42), 11354–11365. https://doi.org/10.1523/JNEUROSCI.0723-07.2007

Dombeck, D. A., Khabbaz, A. N., Collman, F., Adelman, T. L., & Tank, D. W. (2007). Imaging large-scale neural activity with cellular resolution in awake, mobile mice. *Neuron*, *56*(1), 43–57. https://doi.org/10.1016/j.neuron.2007.08.003

El Manira, A. (2014). Dynamics and plasticity of spinal locomotor circuits. *Current Opinion in Neurobiology*, *29*, 133–141. https://doi.org/10.1016/j.conb.2014.06.016

Frohlich, F., Bazhenov, M., Timofeev, I., Steriade, M., & Sejnowski, T. J. (2006). Slow state transitions of sustained neural oscillations by activity-dependent modulation of intrinsic excitability. *The Journal of Neuroscience*, *26*(23), 6153–6162. https://doi.org/10.1523/JNEUROSCI.5509-05.2006

Gourine, A. V., Kasymov, V., Marina, N., Tang, F., Figueiredo, M. F., Lane, S., Teschemacher, A. G., Spyer, K. M., Deisseroth, K., & Kasparov, S. (2010). Astrocytes control breathing through pH-dependent release of ATP. *Science*, *329*(5991), 571–575. https://doi.org/10.1126/science.1190721

Grichtchenko, I., & Chesler, M. (1996). Calcium- and barium-dependent extracellular alkaline shifts evoked by electrical activity in rat hippocampal slices. *Neuroscience*, *75*(4), 1117–1126. https://doi.org/10.1016/0306-4522(96)00293-x

Grillner, S., & El Manira, A. (2020). Current principles of motor control, with special reference to vertebrate locomotion. *Physiological Reviews*, *100*(1), 271–320. https://doi.org/10.1152/physrev.00015.2019

Higashi, K., Fujita, A., Inanobe, A., Tanemoto, M., Doi, K., Kubo, T., & Kurachi, Y. (2001). An inwardly rectifying K+ channel, Kir4.1, expressed in astrocytes surrounds synapses and blood vessels in brain. *American Journal of Physiology. Cell Physiology*, *281*(3), C922–C931. https://doi.org/10.1152/ajpcell.2001.281.3.C922

Jensen, M. S., Azouz, R., & Yaari, Y. (1994). Variant firing patterns in rat hippocampal pyramidal cells modulated by extracellular potassium. *Journal of Neurophysiology*, *71*(3), 831–839. https://doi.org/10.1152/jn.1994.71.3.831

Kelley, K. W., Ben Haim, L., Schirmer, L., Tyzack, G. E., Tolman, M., Miller, J. G., Tsai, H. H., Chang, S. M., Molofsky, A. V., Yang, Y., Patani, R., Lakatos, A., Ullian, E. M., & Rowitch, D. H. (2018). Kir4.1-dependent astrocyte-fast motor neuron interactions are required for peak strength. *Neuron*, *98*(2), 306–319. https://doi.org/10.1016/j.neuron.2018.03.010

Kiehn, O. (2016). Decoding the organization of spinal circuits that control locomotion. *Nature Reviews Neuroscience*, *17*(4), 224–238. https://doi.org/10.1038/nrn.2016.9

Kofuji, P., & Newman, E. A. (2004). Potassium buffering in the central nervous system. *Neuroscience*, *129*(4), 1043–1054. https://doi.org/10.1016/j.neuroscience.2004.06.008

Lee, H. S., Ghetti, A., Pinto-Duarte, A., Wang, X., Dziewczapolski, G., Galimi, F., Huitron-Resendiz, S., Pina-Crespo, J. C., Roberts, A. J., Verma, I. M., Sejnowski, T. J., & Heinemann, S. F. (2014). Astrocytes contribute to gamma oscillations and recognition memory. *Proceedings of the National Academy of Sciences*, *111*(32), E3343–E3352. https://doi.org/10.1073/pnas.1410893111

Li, J., Blankenship, M. L., & Baccei, M. L. (2013). Inward-rectifying potassium (Kir) channels regulate pacemaker activity in spinal nociceptive circuits during early life. *The Journal of Neuroscience*, *33*(8), 3352–3362. https://doi.org/10.1523/JNEUROSCI.4365-12.2013

Ma, Z., Stork, T., Bergles, D. E., & Freeman, M. R. (2016). Neuromodulators signal through astrocytes to alter neural circuit activity and behaviour. *Nature*, *539*(7629), 428–432. https://doi.org/10.1038/nature20145

Masino, M. A., Abbinanti, M. D., Eian, J., & Harris-Warrick, R. M. (2012). TTX-resistant NMDA receptor-mediated membrane potential oscillations in neonatal mouse Hb9 interneurons. *PLoS One*, *7*(10), e47940. https://doi.org/10.1371/journal.pone.0047940

Mazaud, D., Capano, A., & Rouach, N. (2021). The many ways astroglial connexins regulate neurotransmission and behavior. *Glia*, *69*(11), 2527–2545. https://doi.org/10.1002/glia.24040

Montalant, A., Carlsen, E. M. M., & Perrier, J. F. (2021). Role of astrocytes in rhythmic motor activity. *Physiological Reports*, *9*(18), e15029. https://doi.org/10.14814/phy2.15029

Morquette, P., Verdier, D., Kadala, A., Féthière, J., Philippe, A. G., Robitaille, R., & Kolta, A. (2015). An astrocyte-dependent mechanism for neuronal rhythmogenesis. *Nature Neuroscience*, *18*(6), 844–854. https://doi.org/10.1038/nn.4013

Mu, Y., Bennett, D. V., Rubinov, M., Narayan, S., Yang, C. T., Tanimoto, M., Mensh, B. D., Looger, L. L., & Ahrens, M. B. (2019). Glia accumulate evidence that actions are futile and suppress unsuccessful behavior. *Cell*, *178*(1), 27–43. https://doi.org/10.1016/j.cell.2019.05.050

Neprasova, H., Anderova, M., Petrik, D., Vargova, L., Kubinova, S., Chvatal, A., & Sykova, E. (2007). High extracellular K(+) evokes changes in voltage-dependent K(+) and Na (+) currents and volume regulation in astrocytes. *Pflügers Archiv*, *453*(6), 839–849. https://doi.org/10.1007/s00424-006-0151-9

Nimmerjahn, A., Mukamel, E. A., & Schnitzer, M. J. (2009). Motor behavior activates Bergmann glial networks. *Neuron*, *62*(3), 400–412. https://doi.org/10.1016/j.neuron.2009.03.019

Nwaobi, S. E., Cuddapah, V. A., Patterson, K. C., Randolph, A. C., & Olsen, M. L. (2016). The role of glial-specific Kir4.1 in normal and pathological states of the CNS. *Acta Neuropathologica*, *132*(1), 1–21. https://doi.org/10.1007/s00401-016-1553-1

Olsen, M. L., Higashimori, H., Campbell, S. L., Hablitz, J. J., & Sontheimer, H. (2006). Functional expression of Kir4.1 channels in spinal cord astrocytes. *Glia*, *53*(5), 516–528. https://doi.org/10.1002/glia.20312

Otsu, Y., Couchman, K., Lyons, D. G., Collot, M., Agarwal, A., Mallet, J.-M., Pfrieger, F. W., Bergles, D. E., & Charpak, S. (2015). Calcium dynamics in astrocyte processes during neurovascular coupling. *Nature Neuroscience*, *18*(2), 210–218. https://doi.org/10.1038/nn.3906

Panatier, A., Vallée, J., Haber, M., Murai, K. K., Lacaille, J.-C., & Robitaille, R. (2011). Astrocytes are endogenous regulators of basal transmission at central synapses. *Cell*, *146*(5), 785–798. https://doi.org/10.1016/j.cell.2011.07.022

Paukert, M., Agarwal, A., Cha, J., Doze, Van, A., Kang, J. U., & Bergles, D. E. (2014). Norepinephrine controls Astroglial responsiveness to local circuit activity. *Neuron*, *82*(6), 1263–1270. https://doi.org/10.1016/j.neuron.2014.04.038

Poskanzer, K. E., & Yuste, R. (2016). Astrocytes regulate cortical state switching in vivo. *Proceedings of the National Academy of Sciences*, *113*(19), E2675–E2684. https://doi.org/10.1073/pnas.1520759113

Ransom, C. B., & Sontheimer, H. (1995). Biophysical and pharmacological characterization of inwardly rectifying K+ currents in rat spinal cord astrocytes. *Journal of Neurophysiology*, *73*(1), 333–346. https://doi.org/10.1152/jn.1995.73.1.333

Ratto, D., Ferrari, B., Roda, E., Brandalise, F., Siciliani, S., De Luca, F., Priori, E. C., De Iorio, C., Cobelli, F., Veneroni, P., Bottone, M. G., & Rossi, P. (2020). Squaring the circle: A new study of inward and outward-rectifying potassium currents in U251 GBM cells. *Cellular and Molecular Neurobiology*, *40*(5), 813–828. https://doi.org/10.1007/s10571-019-00776-3

Rosa, J. M., Bos, R., Sack, G. S., Fortuny, C., Agarwal, A., Bergles, D. E., Flannery, J. G., & Feller, M. B. (2015). Neuron-glia signaling in

developing retina mediated by neurotransmitter spillover. *eLife*, *4*, e09590. https://doi.org/10.7554/eLife.09590

Savtchouk, I., & Volterra, A. (2018). Gliotransmission: Beyond black-and-white. *The Journal of Neuroscience*, *38*(1), 14–25. https://doi.org/10.1523/JNEUROSCI.0017-17.2017

Sheikhbahaei, S., Turovsky, E. A., Hosford, P. S., Hadjihambi, A., Theparambil, S. M., Liu, B., Marina, N., Teschemacher, A. G., Kasparov, S., Smith, J. C., & Gourine, A. V. (2018). Astrocytes modulate brainstem respiratory rhythm-generating circuits and determine exercise capacity. *Nature Communications*, *9*(1), 370. https://doi.org/10.1038/s41467-017-02723-6

Sibille, J., Dao Duc, K., Holcman, D., & Rouach, N. (2015). The neuroglial potassium cycle during neurotransmission: Role of Kir4.1 channels. *PLoS Computational Biology*, *11*(3), e1004137. https://doi.org/10.1371/journal.pcbi.1004137

Talpalar, A. E., Bouvier, J., Borgius, L., Fortin, G., Pierani, A., & Kiehn, O. (2013). Dual-mode operation of neuronal networks involved in left–right alternation. *Nature*, *500*(7460), 85–88. https://doi.org/10.1038/nature12286

Tazerart, S., Vinay, L., & Brocard, F. (2008). The persistent sodium current generates pacemaker activities in the central pattern generator for locomotion and regulates the locomotor rhythm. *Journal of Neuroscience*, *28*(34), 8577–8589. https://doi.org/10.1523/JNEUROSCI.1437-08.2008

Tong, X., Ao, Y., Faas, G. C., Nwaobi, S. E., Xu, J., Haustein, M. D., Anderson, M. A., Mody, I., Olsen, M. L., Sofroniew, M. V., & Khakh, B. S. (2014). Astrocyte Kir4.1 ion channel deficits contribute to neuronal dysfunction in Huntington's disease model mice. *Nature Neuroscience*, *17*(5), 694–703. https://doi.org/10.1038/nn.3691

Tsai, H.-H., Li, H., Fuentealba, L. C., Molofsky, A. V., Taveira-Marques, R., Zhuang, H., Tenney, A., Murnen, A. T., Fancy, S. P. J., Merkle, F., Kessaris, N., Alvarez-Buylla, A., Richardson, W. D., & Rowitch, D. H. (2012). Regional astrocyte allocation regulates CNS synaptogenesis and repair. *Science*, *337*(6092), 358–362. https://doi.org/10.1126/science.1222381

Verkhratsky, A., Bush, N., Nedergaard, M., & Butt, A. (2018). The special case of human astrocytes. *Neuroglia*, *1*(1), 21–29. https://doi.org/10.3390/neuroglia1010004

Verkhratsky, A., & Nedergaard, M. (2018). Physiology of astroglia. *Physiological Reviews*, *98*(1), 239–389. https://doi.org/10.1152/physrev.00042.2016

Wang, F., Smith, N. A., Xu, Q., Fujita, T., Baba, A., Matsuda, T., Takano, T., Bekar, L., & Nedergaard, M. (2012). Astrocytes modulate neural network activity by Ca2+-dependent uptake of extracellular K+. *Science Signaling*, *5*(218), ra26-ra26. https://doi.org/10.1126/scisignal.2002334

Wang, F., Xu, Q., Wang, W., Takano, T., & Nedergaard, M. (2012). Bergmann glia modulate cerebellar Purkinje cell bistability via Ca2+-−dependent K+ uptake. *Proceedings of the National Academy of Sciences of the United States of America*, *109*(20), 7911–7916. https://doi.org/10.1073/pnas.1120380109

Wilson, J. M., Hartley, R., Maxwell, D. J., Todd, A. J., Kaltschmidt, J. A., Yoshida, Y., Jessell, T. M., & Brownstone, R. M. (2005). Conditional rhythmicity of ventral spinal interneurons defined by expression of the Hb9 homeodomain protein. *Journal of Neuroscience*, *25*(24), 5710–5719. https://doi.org/10.1523/JNEUROSCI.0274-05.2005

Witts, E. C., Nascimento, F., & Miles, G. B. (2015). Adenosine-mediated modulation of ventral horn interneurons and spinal motoneurons in neonatal mice. *Journal of Neurophysiology*, *114*(4), 2305–2315. https://doi.org/10.1152/jn.00574.2014

Xu, H., Cui, N., Yang, Z., Qu, Z., & Jiang, C. (2000). Modulation of Kir4.1 and Kir5.1 by hypercapnia and intracelllular acidosis. *The Journal of Physiology*, *524*(Pt 3), 725–735. https://doi.org/10.1111/j.1469-7793.2000.00725.x

Ziskind-Conhaim, L., Wu, L., & Wiesner, E. P. (2008). Persistent sodium current contributes to induced voltage oscillations in locomotor-related hb9 interneurons in the mouse spinal cord. *Journal of Neurophysiology*, *100*(4), 2254–2264. https://doi.org/10.1152/jn.90437.2008

SUPPORTING INFORMATION

Additional supporting information can be found online in the Supporting Information section at the end of this article.

How to cite this article: Barbay, T., Pecchi, E., Ducrocq, M., Rouach, N., Brocard, F., & Bos, R. (2023). Astrocytic Kir4.1 channels regulate locomotion by orchestrating neuronal rhythmicity in the spinal network. *Glia*, 1–19. https://doi.org/10.1002/glia.24337